Modeling of morphology evolution in the injection molding process of thermoplastic polymers

R. Pantani, I. Coccorullo, V. Speranza, G. Titomanlio *

Department of Chemical and Food Engineering, University of Salerno, via Ponte don Melillo, I-84084 Fisciano (Salerno), Italy

Abstract

A thorough analysis of the effect of operative conditions of injection molding process on the morphology distribution inside the obtained moldings is performed, with particular reference to semi-crystalline polymers. The paper is divided into two parts: in the first part, the state of the art on the subject is outlined and discussed; in the second part, an example of the characterization required for a satisfactorily understanding and description of the phenomena is presented, starting from material characterization, passing through the monitoring of the process cycle and arriving to a deep analysis of morphology distribution inside the moldings. In particular, fully characterized injection molding tests are presented using an isotactic polypropylene, previously carefully characterized as far as most of properties of interest. The effects of both injection flow rate and mold temperature are analyzed. The resulting moldings morphology (in terms of distribution of crystallinity degree, molecular orientation and crystals structure and dimensions) are analyzed by adopting different experimental techniques (optical, electronic and atomic force microscopy, IR and WAXS analysis).

Final morphological characteristics of the samples are compared with the predictions of a simulation code developed at University of Salerno for the simulation of the injection molding process.
© 2005 Elsevier Ltd. All rights reserved.

Contents

---

* Corresponding author. Tel.: +39 089 964152; fax: +39 089 964057.
  E-mail address: gtitomanlio@unisa.it (G. Titomanlio).

1. Introduction

Injection molding is one of the most widely employed methods for manufacturing polymeric products. Three main steps are recognized in the molding: filling, packing/holding and cooling. During the filling stage, a hot polymer melt rapidly fills a cold mold reproducing a cavity of the desired product shape. During the packing/holding stage, the pressure is raised and extra material is forced into the mold to compensate for the effects that both temperature decrease and crystallinity development determine on density during solidification. The cooling stage starts at the solidification of a thin section at cavity entrance (gate), starting from that instant no more material can enter or exit from the mold impression and holding pressure can be released. When the solid layer on the mold surface reaches a thickness sufficient to assure required rigidity, the product is ejected from the mold.

Due to the thermomechanical history experienced by the polymer during processing, macromolecules in injection-molded objects present a local order. This order is referred to as 'morphology' which literally means 'the study of the form' where *form* stands for the shape and arrangement of parts of the object. When referred to polymers, the word morphology is adopted to indicate:

– crystallinity, which is the relative volume occupied by each of the crystalline phases, including mesophases;
– dimensions, shape, distribution and orientation of the crystallites;
– orientation of amorphous phase.

Nomenclature

α	shift factor in the Cross-WLF equation
α'	parameter adopted to describe the iPP T30G viscoelastic behavior
α_{am}	thermal expansion coefficient of the amorphous phase
α_{cr}	thermal expansion coefficient of the crystalline phase
ε	parameter for the heterogeneous nucleation
β_{am}	compressibility factor of the amorphous phase
β_{cr}	compressibility factor of the crystalline phase
χ	overall crystallinity degree
δ	thickness of the oriented region of an injection molded semi-crystalline sample
δ_c	undisturbed volume fraction of the crystals
δ_{ci}	undisturbed volume fraction of the crystals, i-phase
ϕ	maximum eigenvalue of the deformation tensor $\underset{=}{A}$
ψ	parameter for the beterogeneous nucleation
γ'	shear rate
γ	strain
η	melt viscosity
η_0	zero-shear-rate viscosity
η_k	shear viscosity of the kth mode in Leonov model
λ	relaxation time
λ_k	relaxation time of the kth mode in Leonov model
ν	number of Kuhn segments per unit volume
θ	orientation angle
$\underset{=}{\tau}$	stress tensor
$\underset{=}{\sigma}$	molecular strain
ω	frequency
$\xi_{a,final}$	crystallization degree for the alfa phase at the end of the crystallization process
ξ	relative degree of crystallization
ξ_c	critical crystallinity degree: value at which melt viscosity experiences an abrupt increase
ξ_i	relative degree of crystallization, i-phase
ΔG	volumetric free energy difference between molten and crystalline phase
ΔH	latent heat of fusion
$\Delta S(flow)$	change in melt entropy due to the effect of flow
$\underset{=}{1}$	unit tensor
$\underset{=}{\nabla v}$	velocity gradient
$\underset{=}{\mathrm{a}}$	dimensionless parameter for induction time
$\underset{=}{A}$	deformation of the dumbbell subchains population with respect to the equilibrium
a_0, a_1, a_2, a_3	parameters used to describe the effect of crystallinity on viscosity
A_1, A_2	Cross-WLF model parameter
A_{am}	absorbance amorphous phase
a_{am}	absorption coefficient of the amorphous phase peak
A_{cr}	absorbance crystalline phase
a_{cr}	absorption coefficient of the crystalline phase peak
A_i	areas under selected peaks of two-dimensional WAXD patterns
b	parameters adopted to describe the iPP T30G viscoelastic behavior
B	Cross-WLF model parameter
B_1, B_2	parameters adopted to describe the iPP T30G viscoelastic behavior
C_N	proportionality parameter between first normal stress difference and the generation rate of N_s
C	parameter in the Cross-WLF model
c_1, c_2	parameters used for the increment of melt temperature with shear stress
C_1, C_2	nucleation rate parameter for the homogeneous nucleation case
C_k	elastic strain tensor of the kth mode in Leonov model
C_m	shape factor in Kolmogoroff's model
D	kinetic parameter
D_r	Dichroic ratio
D_{r0}	Dichroic ratio for an ideal oriented polymer
D_0	parameter used for the increment of D with shear stress
D_1, D_2	Cross-WLF model parameter
E	parameters adopted to describe the iPP T30G viscoelastic behavior
e_1, e_2	parameter describing the effect of (overall) crystallinity degree on iPP T30G viscoelastic behavior
F	multiplying factor describing the effect of flow on crystallization kinetics
f	Hermans' orientation factor
F_1, F_2	parameters adopted to describe the iPP T30G viscoelastic behavior

f_1, f_2	parameters describing the effect of (overall) crystallinity degree on viscosity
G_S	shear modulus of the polymer
G	spherulitic growth rate
G'	loss modulus
G''	storage modulus
G_0	parameter in Hoffman–Lauritzen expression for the laminar growth rate
h	parameter used for the increment of D with shear stress
h_x	shift factor describing the effect of (overall) crystallinity degree on viscosity
h_χ'	shift factor describing the effect of (overall) crystallinity degree on relaxation time
H_c	enthalpy of the crystalline phases
H_m	enthalpy of the melt phases
K	kinetic constant for crystallinity
K^*	parameter in Hoffman–Lauritzen expression for the kinetic constant
K_0	maximum value of kinetic constant
k_B	Boltzmann constant
K_g	parameter in Hoffman–Lauritzen expression for the growth rate
m	parameter describing the effect of (overall) crystallinity degree on viscosity
M	maximum number of modes in Leonov model
n	Avrami index
N	nucleation density
N_0	nucleation density parameter for the heterogeneous nucleation case
N_1	first normal stress difference
N_a	number of active nuclei
$N_{a,final}$	number of active nuclei at the end of the crystallization process
N_q	number of nuclei per unit volume observed in quiescent condition
N_s	number of nuclei per unit volume induced by the flow
p	parameter describing the effect of (overall)

	crystallinity degree on iPP T30G viscoelastic behavior
P	pressure
q	cooling rate
r	cross-WLF model parameter
$\bar{R}$	final average radius of the spherulites
$\underline{R}$	end-to-end vector of a molecular subchain
$<\underline{R}\underline{R}>$	second-order conformation tensor
$\langle\underline{R}\underline{R}\rangle_0$	second-order conformation tensor under quiescent conditions
$\langle R_0^2\rangle$	end-to-end distance of the molecular chain
R	The universal gas constant
s	rheological constant in Leonov model $(0 < s < 1)$
S	sample thickness
S_c	entropy of the crystalline phases
S_m	entropy of the melt phases
t	time
T	temperature
T_∞	parameter for induction time
T_0	reference temperature in PVT material description
t_{05}	crystallization half-time
t_f	flow characteristic time
T_g	glass transition temperature
t_{ind}	induction time
T_m	melting temperature
t_m	parameter for induction time
T_{max}	temperature of maximum value of kinetic constant
U	parameter in Hoffman–Lauritzen expression for the growth rate
U^*	parameter in Hoffman–Lauritzen expression for the kinetic constant
$\underline{v}$	velocity vector
v	specific volume
v_{oam}	specific volume of a fully amorphous sample
v_{ocr}	specific volume of a fully crystalline sample

Apart from the scientific interest in understanding the mechanisms leading to different order levels inside a polymer, the great technological importance of morphology relies on the fact that polymer characteristics (above all mechanical, but also optical, electrical, transport and chemical) are to a great extent affected by morphology. For instance, crystallinity has a pronounced effect on the mechanical properties of the bulk material since crystals are generally stiffer than amorphous material, and also orientation induces anisotropy and other changes in mechanical properties.

In this work, a thorough analysis of the effect of injection molding operative conditions on morphology distribution in moldings with particular reference to crystalline materials is performed. The aim of the paper is twofold: first, to outline the state of the art on the subject; second, to present an example of the characterization required for a satisfactorily

understanding and description of the phenomena, starting from material description, passing through the monitoring of the process cycle and arriving to a deep analysis of morphology distribution inside the moldings. To these purposes, fully characterized injection molding tests were performed using an isotactic polypropylene, previously carefully characterized as far as most of properties of interest, in particular quiescent nucleation density, spherulitic growth rate and rheological properties (viscosity and relaxation time) were determined. The resulting moldings morphology (in terms of distribution of crystallinity degree, molecular orientation and crystals structure and dimensions) was analyzed by adopting different experimental techniques (optical, electronic and atomic force microscopy, IR and WAXS analysis).

Final morphological characteristics of the samples were compared with the predictions of a simulation code developed at University of Salerno for the simulation of the injection molding process. The effects of both injection flow rate and mold temperature were analyzed.

1.1. Morphology distribution in injection molded iPP parts: state of the art

From many experimental observations, it is shown that a highly oriented lamellar crystallite microstructure, usually referred to as 'skin layer' forms close to the surface of injection molded articles of semi-crystalline polymers. Far from the wall, the melt is allowed to crystallize three dimensionally to form spherulitic structures. Relative dimensions and morphology of both skin and core layers are dependent on local thermo-mechanical history, which is characterized on the surface by high stress levels, decreasing to very small values toward the core region. As a result, the skin and the core reveal distinct characteristics across the thickness and also along the flow path [1].

Structural and morphological characterization of the injection molded polypropylene has attracted the interest of researchers in the past three decades. In the early seventies, Kantz et al. [2] studied the morphology of injection molded iPP tensile bars by using optical microscopy and X-ray diffraction. The microscopic results revealed the presence of three distinct crystalline zones on the cross-section: a highly oriented non-spherulitic skin; a shear zone with molecular chains oriented essentially parallel to the injection direction; a spherulitic core with essentially no preferred orientation. The X-ray diffraction studies indicated that the skin layer

contains biaxially oriented crystallites due to the biaxial extensional flow at the flow front. A similar multilayered morphology was also reported by Menges et al. [3]. Later on, Fujiyama et al. [4] investigated the skin–core morphology of injection molded iPP samples using X-ray Small and Wide Angle Scattering techniques, and suggested that the shear region contains shish–kebab structures. The same shish–kebab structure was observed by Wenig and Herzog in the shear region of their molded samples [5]. A similar investigation was conducted by Titomanlio and co-workers [6], who analyzed the morphology distribution in injection moldings of iPP. They observed a skin–core morphology distribution with an isotropic spherulitic core, a skin layer characterized by a fine crystalline structure and an intermediate layer appearing as a dark band in crossed polarized light, this layer being characterized by high crystallinity. Kalay and Bevis [7] pointed out that, although iPP crystallizes essentially in the α-form, a small amount of β-form can be found in the skin layer and in the shear region. The amount of β-form was found to increase by effect of high shear rates [8]. A wide analysis on the effect of processing conditions on the morphology of injection molded iPP was conducted by Viana et al. [9] and, more recently, by Mendoza et al. [10]. In particular, Mendoza et al. report that the highest level of crystallinity orientation is found inside the shear zone and that a high level of orientation was also found in the skin layer, with an orientation angle tilted toward the core.

It is rather difficult to theoretically establish the relationship between the observed microstructure and processing conditions. Indeed, a model of the injection molding process able to predict morphology distribution in the final samples is not yet available, even if it would be of enormous strategic importance. This is mainly because a complete understanding of crystallization kinetics in processing conditions (high cooling rates and pressures, strong and complex flow fields) has not yet been reached.

In this section, the most relevant aspects for process modeling and morphology development are identified. In particular, a successful path leading to a reliable description of morphology evolution during polymer processing should necessarily pass through:

– a good description of morphology evolution under quiescent conditions (accounting all competing crystallization processes), including the range of cooling rates characteristic of processing operations (from 1 to 1000 °C/s);

– a description capturing the main features of melt morphology (orientation and stretch) evolution under processing conditions;
– a good coupling of the two (quiescent crystallization and orientation) in order to capture the effect of crystallinity on viscosity and the effect of flow on crystallization kinetics.

The points listed above outline the strategy to be followed in order to achieve the basic understanding for a satisfactory description of morphology evolution during all polymer processing operations. In the following, the state of art for each of those points will be analyzed in a dedicated section.

1.1.1. Modeling of the injection molding process

The first step in the prediction of the morphology distribution within injection moldings is obviously the thermo-mechanical simulation of the process. Much of the efforts in the past were focused on the prediction of pressure and temperature evolution during the process and on the prediction of the melt front advancement [11–15]. The simulation of injection molding involves the simultaneous solution of the mass, energy and momentum balance equations. The fluid is non-Newtonian (and viscoelastic) with all parameters dependent upon temperature, pressure, crystallinity, which are all function of time. Compressibility cannot be neglected as the flow during the packing/holding step is determined by density changes due to temperature, pressure and crystallinity evolution.

Indeed, apart from some attempts to introduce a full 3D approach [16–19], the analysis is currently still often restricted to the Hele–Shaw (or thin film) approximation, which is warranted by the fact that most injection molded parts have the characteristic of being thin. Furthermore, it is recognized that the viscoelastic behavior of the polymer only marginally influences the flow kinematics [20–22] thus the melt is normally considered as a non-Newtonian viscous fluid for the description of pressure and velocity gradients evolution. Some examples of adopting a viscoelastic constitutive equation in the momentum balance equations are found in the literature [23], but the improvements in accuracy do not justify a considerable extension of computational effort.

It has to be mentioned that the analysis of some features of kinematics and temperature gradients affecting the description of morphology need a more accurate description with respect to the analysis of pressure distributions. Some aspects of the process which were often neglected and may have a critical

importance are the description of the heat transfer at polymer–mold interface [24–26] and of the effect of mold deformation [24,27,28].

Another aspect of particular interest to the development of morphology is the fountain flow [29–32], which is often neglected being restricted to a rather small region at the flow front and close to the mold walls.

1.1.2. Modeling of the crystallization kinetics

It is obvious that the description of crystallization kinetics is necessary if the final morphology of the molded object wants to be described. Also, the development of a crystalline degree during the process influences the evolution of all material properties like density and, above all, viscosity (see below). Furthermore, crystallization kinetics enters explicitly in the generation term of the energy balance, through the latent heat of crystallization [26,33]. It is therefore clear that the crystallinity degree is not only a result of simulation but also (and above all) a phenomenon to be kept into account in each step of process modeling. In spite of its dramatic influence on the process, the efforts to simulate the injection molding of semi-crystalline polymers are crude in most of the commercial software for processing simulation and rather scarce in the literature. Lafleur and Kamal [34], Papatanasiu [35], Titomanlio et al. [15], Han and Wang [36], Ito et al. [37], Manzione [38], Guo and Isayev [26], and Hieber [25] adopted the following equation (Kolmogoroff–Avrami–Evans, KAE) to predict the development of crystallinity

$$\frac{d\xi}{dt} = (1-\xi)\frac{d\delta_c}{dt} \tag{1}$$

where ξ is the relative degree of crystallization; δ_c is the undisturbed volume fraction of the crystals (if no impingement would occur).

A significant improvement in the prediction of crystallinity development was introduced by Titomanlio and co-workers [39] who kept into account the possibility of the formation of different crystalline phases. This was done by assuming a parallel of several non-interacting kinetic processes competing for the available amorphous volume. The evolution of each phase can thus be described by

$$\frac{d\xi_i}{dt} = (1-\xi)\frac{d\delta_{ci}}{dt} \tag{2}$$

where the subscript i stands for a particular phase, ξ_i is the relative degree of crystallization, $\xi = \sum_i \xi_i$ and $\delta_{c\ i}$

is the expectancy of volume fraction of each phase if no impingement would occur.

Eq. (2) assumes that, for each phase, the probability of the fraction increase of a single crystalline phase is simply the product of the rate of growth of the corresponding undisturbed volume fraction and of the amount of available amorphous fraction.

By summing up the phase evolution equations of all phases (Eq. (2)) over the index *i*, and solving the resulting differential equation, one simply obtains

$$\xi(t) = 1 - \exp[-\delta_c(t)] \tag{3}$$

where $\delta_c = \sum_i \delta_{ci}$ and Eq. (1) is recovered.

It was shown by Coccorullo et al. [40] with reference to an iPP, that the description of the kinetic competition between phases is crucial to a reliable prediction of solidified structures: indeed, it is not possible to describe iPP crystallization kinetics in the range of cooling rates of interest for processing (i.e. up to several hundreds of °C/s) if the mesomorphic phase is neglected: in the cooling rate range 10–100 °C/s, spherulite crystals in the α-phase are overcome by the formation of the mesophase. Furthermore, it has been found that in some conditions (mainly at pressures higher than 100 MPa, and low cooling rates), the γ-phase can also form [41]. In spite of this, the presence of different crystalline phases is usually neglected in the literature, essentially because the range of cooling rates investigated for characterization falls in the DSC range (well lower than typical cooling rates of interest for the process) and only one crystalline phase is formed for iPP at low cooling rates.

It has to be noticed that for iPP, which presents a T_g well lower than ambient temperature, high values of crystallinity degree are always found in solids which passed through ambient temperature, and the cooling rate can only determine which crystalline phase forms, roughly α-phase at low cooling rates (below about 50 °C/s) and mesomorphic phase at higher cooling rates.

The most widespread approach to the description of kinetic constant is the isokinetic approach introduced by Nakamura et al. According to this model, δ_c in Eq. (1) is calculated as

$$\delta_c(t) = \ln 2 \left[\int_0^t K(T(s)) \mathrm{d}s \right]^n \tag{4}$$

where K is the kinetic constant and n is the so-called Avrami index. When introduced as in Eq. (4), the reciprocal of the kinetic constant is a characteristic time

for crystallization, namely the crystallization half-time, t_{05}. If a polymer is cooled through the crystallization temperature, crystallization takes place at the temperature at which crystallization half-time is of the order of characteristic cooling time t_q defined as

$$t_q = \Delta T/q \tag{5}$$

where q is the cooling rate and ΔT is a temperature interval over which the crystallization kinetic constant changes of at least one order of magnitude.

The temperature dependence of the kinetic constant is modeled using some analytical function which, in the simplest approach, is described by a Gaussian shaped curve:

$$K(T) = K_0 \exp\left[-4 \ln 2 \frac{(T - T_{max})^2}{D^2} \right] \tag{6}$$

The following Hoffman–Lauritzen expression [42] is also commonly adopted:

$$K[T(t)] = K_0 \exp\left[-\frac{U^*}{R \cdot (T(t) - T_\infty)} \right]$$
$$\times \exp\left[-\frac{K^* \cdot (T(t) + T_m)}{2T(t)^2 \cdot (T_m - T(t))} \right] \tag{7}$$

Both equations describe a bell shaped curve with a maximum which for Eq. (6) is located at $T = T_{max}$ and for Eq. (7) lies at a temperature between T_m (the melting temperature) and T_∞ (which is classically assumed to be 30 °C below the glass transition temperature). According to Eq. (7), the kinetic constant is exactly zero at $T = T_m$ and at $T = T_\infty$, whereas Eq. (6) describes a reduction of several orders of magnitude when the temperature departs from T_{max} of a value higher than 2D. It is worth mentioning that only three parameters are needed for Eq. (6), whereas Eq. (7) needs the definition of five parameters. Some authors [43,44] couple the above equations with the so-called 'induction time', which can be defined as the time the crystallization process starts, when the temperature is below the equilibrium melting temperature. It is normally described as [45]

$$\frac{Dt_{ind}}{Dt} = \frac{(T_m^0 - T)^a}{t_m} \tag{8}$$

where t_m, T_m^0 and a are material constants. It should be mentioned that it has been found [46,47] that there is no need to explicitly incorporate an induction time when the modeling is based upon the KAE equation (Eq. (1)).

1.1.3. Modeling of the morphology evolution

Despite of the fact that the approaches based on Eq. (4) do represent a significant step toward the description

of morphology, it has often been pointed out in the literature that the isokinetic approach on which Nakamura's equation (Eq. (4)) is based does not describe details of structure formation [48]. For instance, the well-known experience that, with many polymers, the number of spherulites in the final solid sample increases strongly with increasing cooling rate, is indeed not taken into account by this approach. Furthermore, Eq. (4) describes an increase of crystallinity (at constant temperature) depending only on the current value of crystallinity degree itself, whereas it is expected that the crystallization rate should depend also on the number of crystalline entities present in the material.

These limits are overcome by considering the crystallization phenomenon as the consequence of nucleation and growth. Kolmogoroff's model [49], which describes crystallinity evolution accounting of the number of nuclei per unit volume and spherulitic growth rate can then be applied. In this case, δ_c in Eq. (1) is described as

$$\delta(t) = C_m \int_0^t \frac{dN(s)}{ds} \cdot \left[\int_s^t G(u)du\right]^n ds \tag{9}$$

where C_m is a shape factor ($C_3 = 4/3\pi$, for spherical growth), $G(T(t))$ is the linear growth rate, and $N(T(t))$ is the nucleation density.

The following Hoffman–Lauritzen expression is normally adopted for the growth rate

$$G[T(t)] = G_0 \exp\left[-\frac{U}{R\cdot(T(t) - T_\infty)}\right]$$
$$\times \exp\left[-\frac{K_g\cdot(T(t) + T_m)}{2T(t)^2\cdot(T_m - T(t))}\right] \tag{10}$$

Eqs. (7) and (10) have the same form, however the values of the constants are different.

The nucleation mechanism can be either homogeneous or heterogeneous. In the case of heterogeneous nucleation, two equations are reported in the literature, both describing the nucleation density as a function of temperature [37,50]:

$$N(T(t)) = N_0 \exp[\psi\cdot(T_m - T(t))] \tag{11}$$

$$N(T(t)) = N_0 \exp\left[-\varepsilon\cdot\frac{T_m}{T(t)(T_m - T(t))}\right] \tag{12}$$

In the case of homogeneous nucleation, the nucleation rate rather than the nucleation density is function of temperature, and a Hoffman–Lauritzen expression is

adopted

$$\frac{dN(T(t))}{dt} = N_0 \exp\left[-\frac{C_1}{(T(t) - T_\infty)}\right]$$
$$\times \exp\left[-\frac{C_2\cdot(T(t) + T_m)}{T(t)^2\cdot(T_m - T(t))}\right] \tag{13}$$

Concentration of nucleating particles is usually quite significant in commercial polymers, and thus heterogeneous nucleation becomes the dominant mechanism.

When Kolmogoroff's approach is followed, the number N_a of active nuclei at the end of the crystallization process can be calculated as [48]

$$N_{a,\text{final}} = \int_0^{t_{\text{final}}} \frac{dN[T(s)]}{ds}(1 - \xi(s))ds \tag{14}$$

and the average dimension of crystalline structures can be attained by geometrical considerations. Pantani et al. [51] and Zuidema et al. [22] exploited this method to describe the distribution of crystallinity and the final average radius of the spherulites in injection moldings of polypropylene; in particular, they adopted the following equation

$$\bar{R} = \sqrt[3]{\frac{3\xi_{\alpha,\text{final}}}{4\pi N_{a,\text{final}}}} \tag{15}$$

A different approach is also present in the literature, somehow halfway between Nakamura's and Kolmogoroff's models: the growth rate (G) and the kinetic constant (K) are described independently, and the number of active nuclei (and consequently the average dimensions of crystalline entities) can be obtained by coupling Eqs. (4) and (9) as

$$N_a(T) = \frac{3\ln 2}{4\pi}\left[\frac{K(T)}{G(T)}\right]^3 \tag{16}$$

where heterogeneous nucleation and spherical growth is assumed (Avrami's index = 3). Guo et al. [43] adopted this approach to describe the dimensions of spherulites in injection moldings of polypropylene.

1.1.4. Modeling of the effect of crystallinity on rheology

As mentioned above, crystallization has a dramatic influence on material viscosity. This phenomenon must obviously be taken into account and, indeed, the solidification of a semi-crystalline material is essentially caused by crystallization rather than by temperature in normal processing conditions.

Despite of the importance of the subject, the relevant literature on the effect of crystallinity on viscosity is

rather scarce. This might be due to the difficulties in measuring simultaneously rheological properties and crystallinity evolution during the same tests. Apart from some attempts to obtain simultaneous measurements of crystallinity and viscosity by special setups [52,53], more often viscosity and crystallinity are measured during separate tests having the same thermal history, thus greatly simplifying the experimental approach. Nevertheless, very few works can be retrieved in the literature in which (shear or complex) viscosity can be somehow linked to a crystallinity development. This is the case of Winter and co-workers [54], Vleeshouwers and Meijer [55] (crystallinity evolution can be drawn from Swartjes [56]), Boutahar et al. [57], Titomanlio et al. [15], Han and Wang [36], Floudas et al. [58], Wassner and Maier [59], Pantani et al. [60], Pogodina et al. [61], Acierno and Grizzuti [62].

All the authors essentially agree that melt viscosity experiences an abrupt increase when crystallinity degree reaches a certain 'critical' value, ξ_c [15]. However, little agreement is found in the literature on the value of this critical crystallinity degree: assuming that ξ_c is reached when the viscosity increases of one order of magnitude with respect to the molten state, it is found in the literature that, for iPP, ξ_c ranges from a value of a few percent [15,62,60,58] up to values of 20–30% [58,61] or even higher than 40% [59,54,57].

Some studies are also reported on the secondary effects of relevant variables such as temperature or shear rate (or frequency) on the dependence of crystallinity on viscosity. As for the effect of temperature, Titomanlio [15] found for an iPP that the increase of viscosity for the same crystallinity degree

was higher at lower temperatures, whereas Winter [63] reports the opposite trend for a thermoplastic elastomeric polypropylene. As for the effect of shear rate, a general agreement is found in the literature that the increase of viscosity for the same crystallinity degree is lower at higher deformation rates [62,61,57].

Essentially, the equations adopted to describe the effect of crystallinity on viscosity of polymers can be grouped into two main categories:

– equations based on suspensions theories (for a review, see [64] or [65]);
– empirical equations.

Some of the equations adopted in the literature with regard to polymer processing are summarized in Table 1.

Apart from Eq. (17) adopted by Katayama and Yoon [66], all equations predict a sharp increase of viscosity on increasing crystallinity, sometimes reaching infinite (Eqs. (18) and (21)). All authors consider that the relevant variable is the volume occupied by crystalline entities (i.e. ξ), even if the dimensions of the crystals should reasonably have an effect.

1.1.5. Modeling of the molecular orientation

One of the most challenging problems to present day polymer science regards the reliable prediction of molecular orientation during transformation processes. Indeed, although pressure and velocity distribution during injection molding can be satisfactorily described by viscous models, details of the viscoelastic nature of the polymer need to be accounted for in the description

Table 1
List of the most used equations to describe the effect of crystallinity on viscosity

Equation		Author	Derivation	Parameters
$\eta/\eta_0 = 1 + a_0\xi$	(17)	Katayama [66]	Suspensions	$a = 99$
$\eta/\eta_0 = 1/(\xi - \xi_c)^{a0}$	(18)	Ziabicki [67]	Empirical	$\xi_c = 0.1$
$\eta/\eta_0 = 1 + a_1 \exp(-a_2/\xi^{a3})$	(19)	Titomanlio [15], also adopted by Guo [68] and Hieber [25]	Empirical	
$\eta/\eta_0 = \exp(a_1\xi^{a2})$	(20)	Shimizu [69], also adopted by Zuidema [22] and Hieber [25]	Empirical	
$\eta/\eta_0 = 1 + (\xi/a_1)^{a2}/(1$ $- (\xi/a_1)^{a2})$	(21)	Tanner [70]	Empirical, based on suspensions	$a_1 = 0.44$ for compact crystallites
$\eta/\eta_0 = \exp(a_1\xi + a_2\xi^2)$	(22)	Han [36]	Empirical	$a_1 = 0.68$ for spherical crystallites
$\eta/\eta_0 = 1 + a_1\xi + a_2\xi^2$	(23)	Tanner [71]	Empirical	$a_1 = 0.54$, $a_2 = 4$, $\xi < 0.4$
$\eta/\eta_0 = (1 - \xi/a_0)^{-2}$	(24)	Metzner [65], also adopted by Tanner [70]	Suspensions	$a = 0.68$ for smooth spheres

of the evolution of molecular orientation. From a qualitative point of view, the alignment of macromolecules along a preferred direction is the result of a competition between the characteristic relaxation time, λ, which is a function of thermomechanical and crystallinity histories, and the flow characteristic time, t_f, which is the reciprocal of the deformation rate. High orientation levels can be reached when the ratio t_f/λ is high.

Several approaches are found in the literature regarding the modeling of molecular orientation. In most of relevant literature works, the Leonov constitutive equation was adopted, but also upper convected Maxwell models and, more recently, Pom–Pom model [72,73] have been successfully applied. In this work only the Leonov model and a recently proposed non-linear Dumbbell model are briefly presented in the following.

1.1.5.1. Leonov model. According to this model, the stress tensor can be described as

$$\underline{\underline{\tau}} = -P\underline{\underline{1}} + s\eta_0(\underline{\underline{\nabla v}} + \underline{\underline{\nabla v}}^{\mathrm{T}}) + \sum_{k=1}^{M} \frac{\eta_k}{\lambda_k}\underline{\underline{C_k}} \qquad (25)$$

where η_0 is the zero-shear-rate viscosity, η_k is the shear viscosity of the k th mode, λ_k the relaxation time of the k th mode, and s a rheological constant ($0 < s < 1$); M is the number of modes, $\underline{\underline{1}}$ the unit tensor, v is the velocity vector and $\underline{\underline{\nabla v}}$ is the velocity gradient.

$\underline{\underline{C_k}}$ is the elastic strain tensor of the k th mode, whose evolution with time is described by the following equations

$$\partial\frac{\underline{\underline{C_k}}}{\partial t} + \underline{v}\cdot\underline{\underline{\nabla C_k}} - \underline{\underline{\nabla v}}^{\mathrm{T}}\cdot\underline{\underline{C_k}} - \underline{\underline{C_k}}\cdot\underline{\underline{\nabla v}} + \frac{1}{2\lambda_k}(\underline{\underline{C_k}}\cdot\underline{\underline{C_k}} - \underline{\underline{1}}) = 0 \qquad (26)$$

$$\det \overline{\overline{C_k}} = 1 \qquad (27)$$

Isayev and Hieber [74] analyzed the injection molding process and predicted birefringence distributions in injection-molded PS samples, by considering the stress-optical rule; Baaijens and Douven [75] applied a compressible version of the Leonov model (i.e. releasing the constraint given by Eq. (27)) to calculate the development of orientation in injection molded rectangular strips. Flaman [28] adopted the same approach to predict frozen-in birefringence in an injection molded strip; more recently, Kwon [23] applied the Leonov model to describe experimental

data of birefringence distribution along thickness in centre-gated PS disks.

1.1.5.2. Non-linear dumbbell model. A different viscoelastic equation was adopted by Pantani et al. [20,76], who compared different choices of accounting for non-linearities in the dumbbell model to describe the evolution of molecular orientation in PS samples.

If $\underline{R}$ is the end-to-end vector of a molecular sub chain, and the symbol $\langle\ \rangle$ denotes the average over the configuration space, it is possible to define the fractional 'deformation' of the population of dumbbell sub chains with respect to the equilibrium conformation as

$$\underline{\underline{A}} = \frac{3}{\langle R_0^2\rangle}[\langle\underline{R}\underline{R}\rangle - \langle\underline{R}\underline{R}\rangle_0] \qquad (28)$$

where $\langle\underline{R}\underline{R}\rangle$ is the second-order conformation tensor, $\langle\underline{R}\underline{R}\rangle_0$ is the value of $\langle\underline{R}\underline{R}\rangle$ under quiescent conditions, when the end-to-end distance of the molecular chain is $\langle R_0^2\rangle = \mathrm{tr}\langle\underline{R}\underline{R}\rangle_0$

According to this definition, the constitutive equation for the sub-chain population can be written as

$$\frac{D}{Dt}\underline{\underline{A}} - \underline{\underline{\nabla v}}^{\mathrm{T}}\cdot\underline{\underline{A}} - \underline{\underline{A}}\cdot\underline{\underline{\nabla v}} = -\frac{1}{\lambda}\underline{\underline{A}} + \underline{\underline{\nabla v}} + \underline{\underline{\nabla v}}^{\mathrm{T}} \qquad (29)$$

where $\overline{\overline{\nabla v}}$ is the velocity gradient and λ is the relaxation time.

The polymer contribution to the stress tensor is obtained from the fractional 'deformation' tensor as

$$\underline{\underline{\tau}} = G_S\cdot\underline{\underline{A}} \qquad (30)$$

where G_S is the modulus of the polymer.

In the elastic Dumbbell model the relaxation time, λ, is considered constant and it is well known that with this choice the model is not able to predict the shear thinning behavior of polymer melts. It was shown in the literature [76,77] that, if λ and G are allowed to vary with shear rate and temperature, the consistency between a shear thinning steady-state viscosity and by Eqs. (29) and (30) can be recovered. In particular, the following functions were suggested for the relaxation time [20]

$$\lambda(T, P, \gamma', \chi) = \frac{\lambda\alpha'(T, P, \chi)}{1 + E[\lambda\alpha'(T, P, \chi)\gamma']^{1-b}} \qquad (31)$$

$$\alpha'(T, P, \chi) = 10^{-(F_1(T-B_1-B_2P))/(F_2+T-B_1))}h'_\chi(\chi) \qquad (32)$$

$$h'_\chi(\chi) = \left[1 + e_1 \exp\left(-\frac{e_2}{\chi^p}\right)\right] \tag{33}$$

It is worth mentioning that, according to the model depicted above, material viscoelastic behavior is described with the use of only one relaxation time. However, since relaxation time is taken function of shear rate, it essentially describes a series of infinite relaxation modes, each one playing a role at a given shear rate.

1.1.6. Modeling of the flow-induced crystallization

The phenomenon of strain-induced crystallization is known from the crystallization of rubber. Plenty of works in the literature report a substantial increase of crystallization kinetics of polymers when some level of deformation is imposed to the melt.

Two aspects of the problem deserve attention. On one side, on the basis of above discussions, it is clear that the enhancement of crystallization kinetics has a critical relevance on process modeling. On the other side, it is known that the morphology of the crystals obtained from a strained melt can be very different from that obtained from a fully relaxed quiescent liquid. For example, isotropically grown spherulites are replaced in the latter case by row nuclei overgrown by densely packed or irregularly spaced lamellae (shish–kebabs), giving rise to highly anisotropic structures.

Qualitative features of the effect of flow on crystallization can be summarized as:

– above a critical value of deformation rate, crystallization kinetics increases and an oriented crystalline phase solidifies [62];
– above a second, higher critical value of deformation rate, crystalline structures change from spherulitic to fibrillar [78];
– the orientation of crystalline structures is generally higher than the orientation of the melt [79];
– in samples solidified under flow, the orientation of crystalline structures is generally higher than the orientation of the amorphous phase [80].

As usual when the physics of the phenomenon is not well understood, several approaches are found in the literature, as summarized in the following. It will be noticed that quite different approaches are available in the literature, all of them aimed at improving, by means of a proper choice of a few parameters, the description of crystallinity development in a particular, often quite restricted, set of conditions. Furthermore, most of data are gathered under shear conditions. Obviously, in order to understand which one of the proposed models is the best candidate to describe the effect of flow on crystallization kinetics, or if a new model needs to be developed, it would be necessary to test all models on a much wider set of data of crystallization kinetics both in quiescent and in flow conditions, under wide ranges of both cooling rates and flow histories.

1.1.6.1. Approaches based on Nakamura's model. Many authors modeled the effect of flow on crystallization kinetics by adopting the isokinetic approach introduced by Nakamura. The final formulation of this model does not take into account morphology development. Similarly, all the approaches based on this model consider only the total crystallinity index, and neglect morphology development.

Enhancement of kinetics equation by a multiplying factor function of stress. Doufas et al. [81] modified the crystallization kinetic constant to include the effect of stress on the crystallization of nylon in the melt-spinning process; they introduced a multiplying factor proportional to $F = \exp(\mathrm{tr}(\tau/G_0))$ in the kinetic constant reported in Eq. (4), where τ is the extra stress tensor.

Enhancement of kinetics equation by a multiplying factor function of shear rate. Tanner [70,71] considered the effect of flow on crystallization kinetics of an iPP, by introducing a multiplying factor function of shear rate, $F(\gamma') = 1 + (\gamma'/\gamma'_c)^{1.35}$ with $\gamma'_c = 1.12 \times 10^{-3}$ s^{-1}, obtained by fitting the data presented by Bouthar [57].

Enhancement of kinetics equation by a multiplying factor function of strain. Describing the data presented by Wassner and Maier, Tanner [71] introduced also a multiplying factor function of strain, $F = (1 + a|\gamma|^m)$ where $\gamma = \gamma' t$.

Kulkarni and Beris [82] also considered a strain criterion for crystallization, but their multiplying factor was based on molecular strain derived from rubber elasticity: $F = \exp[A(\sigma^2 + 2/\sigma - 3)]$, where σ is the molecular strain.

Enhancement of kinetics equation by a multiplying factor function of orientation. Ziabicki [83] considered a multiplying factor to the kinetic constant function of the Hermans' orientation factor f: $F = \exp(A(T)f^2)$. It is interesting to notice that applying the stress-optical rule, f can be linearly converted to stress; the multiplying factor becomes thus stress-dependent.

Increase of melting temperature: melting temperature function of stress. The modeling of the effect of flow on crystallization kinetics can be based on chain extension analysis since chain extension causes a decrease in polymeric melt entropy, which on its turn causes an increase in crystallization temperature, and

a parallel increase in crystallization kinetics. At the melting temperature, the free energy of the crystals equals the free energy of the melt so that the melting temperature may be written as

$$T_{\mathrm{m}} = (H_{\mathrm{m}} - H_{\mathrm{c}})/(S_{\mathrm{m}} - S_{\mathrm{c}}) \qquad (34)$$

where H_{m}, S_{m}, H_{c} and S_{c} are enthalpies and entropies of the melt and crystalline phases, respectively.

Eq. (34) can be easily arranged to give

$$T_{\mathrm{m}}(\mathrm{flow}) = \frac{\Delta H^{\circ}}{\Delta H^{\circ} - T_{\mathrm{m}}^{\circ}\,\Delta S(\mathrm{flow})}\,T_{\mathrm{m}}^{\circ} \qquad (35)$$

where $^{\circ}$ stands for quiescent condition, ΔH is the latent heat of fusion (assumed not to change with flow) and $\Delta S(\mathrm{flow})$ is the change in melt entropy due to the effect of flow. The meaning and the consequences of Eq. (35) are such that, for an oriented melt, the decrease in entropy causes an increase of the melting temperature and, therefore, at a given temperature, an increase of supercooling [84].

By assuming that the free energy due to deformation is essentially related to its elastic properties, Haas and Maxwell [85] obtained the following expression for the increase of melting temperature for a stressed polymer melt

$$T_{\mathrm{m}} = T_{\mathrm{m}}^{\circ}(1 + \tau^{2}/2G_{\mathrm{S}}\,\Delta H_{\mathrm{f}}) \qquad (36)$$

where τ is the stress and G_{S} is the modulus of the polymer assumed to be not a function of stress. Eq. (36) relates the increase of melting temperature to the current value of the stress.

The effect of an increase of T_{m} is toward an increase of crystallization kinetics: if a Hoffman–Lauritzen expression is adopted for crystallization kinetic constant, T_{m} is explicitly considered; if a Gaussian expression (Eq. (6)) is considered, either $T_{\max}$ or D are function of T_{m}.

Titomanlio et al. [15] considered indeed that the parameter D of Eq. (6) increases with shear stress according to the equation

$$D = D_{0} + h\tau^{\mathrm{g}} \qquad (37)$$

and found that $g = 1.2$ accommodated the data gathered on an iPP. Eq. (37) was also adopted by Hieber [25].

Guo and Nahr [86] adopted and Hoffman–Lauritzen expression with T_{m} function of stress according to the equation

$$T_{\mathrm{m}} = T_{\mathrm{m}}^{\circ} + c_{1}\exp(-c_{2}/\tau) \qquad (38)$$

The effect of the increase of T_{m} was considered by Guo and Nahr also in the induction time.

Melting temperature function of molecular strain. Both Ito et al. [37] and Titomanlio and Lamberti [87] considered the effect of a melting temperature rise in a Hoffman–Lauritzen expression. They explicitly considered the change of entropy due to deformation according to rubber elasticity

$$\Delta S(\mathrm{flow}) = k_{\mathrm{B}}\nu/2(\sigma^{2} + 2/\sigma - 3) \qquad (39)$$

where k_{B} is the Boltzmann constant, ν is the number of Kuhn segments per unit volume and σ is the molecular strain.

A similar approach was more recently followed by Kim et al. [88].

1.1.6.2. Morphology-oriented approaches. Another group of authors modeled the effect of flow on crystallization kinetics by considering nucleation and growth. The effect of flow on nucleation is toward a dramatic increase of nuclei when the melt undergoes a deformation [89]. Furthermore, the effect of flow on growth rate is still under investigation: some authors observed an increase of growth rate in deformed melt [90], whereas others report that growth rate is not changed by flow [91]. The reason of this discrepancy can rely on the effect of material tacticity [92] or on the presence of a threshold below which the effect of deformation is negligible.

Enhancement of nucleation rate (or of nucleation density). Eder and Janeschitz-Kriegl [48] considered that crystallization of rod nuclei are generated with a rate function of shear rate. They assumed that the nucleation rate follows the following equation

$$\frac{\mathrm{d}N(T(t))}{\mathrm{d}t} = A_{N} - \frac{N(T)}{B_{N}} \qquad (40)$$

in which $A_{N} = g_{N}(T)(\gamma'/\gamma'_{c})^{2}$. The last term of Eq. (40) was neglected due to the high value of the parameter B_{N}.

Zuidema et al. [22] also considered Eq. (40), but replaced the function of shear rate with the second invariant of the deviatoric part of the recoverable strain tensor. This approach has obviously stronger physical basis, since the effect of flow is present also when the deformation rate gets to zero.

It is interesting to notice that the authors [22] considered the flow-induced crystallization as a mechanism in parallel and competing with quiescent crystallization for the available amorphous, within a scheme similar to that considered by Eqs. (2) and (3).

Kosher and Fuchiron [93] also considered that flow promotes an enhancement of nucleation. They assumed

that the number of activated nuclei can be written as the sum of the nuclei observed in quiescent condition N_q, and the nuclei induced by the flow N_s, which are generated at a rate proportional to the first normal stress difference

$$\dot{N}_S = C_N \cdot N_1$$

Enhancement of crystallization kinetics on the basis of free energy considerations. Grizzuti et al. [94] considered the following form of the Hoffman–Lauritzen equation for nucleation rate, where the volumetric free energy difference between molten and crystalline phases, ΔG, appears explicitly

$$\dot{N} = C k_B T \, \Delta G \exp\left(-\frac{E_a}{k_B T}\right) \exp\left(-\frac{K}{T(\Delta G)^n}\right) \qquad (41)$$

The expression adopted for ΔG of a flowing melt was drawn from Doi–Edwards model. ΔG increases by effect of flow, the supercooling increases with it and enhances the nucleation rate by means of a multiplying factor

Zhang and Kennedy [95], considered Eq. (40), but replaced the function of shear rate with a function of the flow-induced free energy f

$$
\begin{aligned}
f(\Delta F_f, T) =& C_0 k_B T \exp\left[-\frac{U^*}{R \cdot (T - T_\infty)}\right]\left\{(\Delta F_q + \Delta F_f)\right. \\
&\times \exp\left[-\frac{K_g}{T \cdot [(1 + \vartheta \, \Delta F_f)T_m^\circ - T]}\right] - \Delta F_q \\
&\times \left.\exp\left[-\frac{K_g}{T \cdot \Delta T}\right]\right\}, \qquad \Delta F_q = \Delta H_0 \Delta T / T_m^\circ, \\
&\times \vartheta = T_m^\circ / \Delta H_0 T
\end{aligned}
\qquad (42)
$$

where C_0 is a fitting parameter, k_B is the Boltzmann's constant, ΔH_0 is the latent heat of crystallization. Eq. (42) is quite similar to Eq. (41) adopted by Grizzuti et al. [94].

The authors also proposed that the index n in Kolmogoroff equation should be a function of the orientation of the semi-crystalline phase calculated by a rigid dumbbell model distribution, and in particular of the second invariant of the second-order orientation tensor

$$n = 4 - 3\langle \underline{R}\underline{R}\rangle : \langle \underline{R}\underline{R}\rangle \qquad (43)$$

where the double dot symbol ':' stands for the scalar product of two tensors.

With this expression, n equals 3 at a random orientation state, corresponding to the spherical growth; and equals 1 at the perfectly aligned orientation state, corresponding to the rod-like growth.

1.2. Comments on the state of the art

Despite of the huge effort spent, the description of the evolution of morphology in injection molding is still challenging. It results clear from the cited literature that most of the research groups working in the area of polymer processing made an independent choice regarding the effect of crystallinity on viscosity and, above all, on the description of the flow induced crystallization phenomenon. In the latter area, essentially, the attitude of the researchers was to improve the description of a particular set of experimental data, trying to relate the enhancement factors to an easily accessible variable: from the simplest possible choice which is obviously the shear rate, to a choice based on more sound physical basis, namely the stress tensor, and to probably the best option which is based on energy (or entropy) functions. It is however still questionable which variable is the most suitable to describe the effect of flow on crystallization kinetics and morphology evolution.

Many are the reasons that avoided a more structured experimental approach and, thus, a modeling activity progressing on a solid and structured experimental information; probably the most significant reasons are:

– the problem cannot be easily split into simple mechanisms, since each of the elementary processes (namely evolution of crystallinity, evolution of orientation, flow fields) strictly interact;
– the experimental conditions on which the elementary models (for quiescent evolution of morphology during crystallization, evolution of structure in the melt, effect of crystallinity on rheology, effect of flow on crystallization kinetics and rheology) are tuned cover very limited ranges of experimental conditions, in terms of pressure, cooling rates and flow fields which in the injection molding process reach very drastic conditions (up to one hundred of MPa, several hundreds of °C/s, and thousands of reciprocal seconds, respectively);
– the sets of data presented in the literature are often incomplete or not fully characterized, thus they cannot be adopted by other researchers to complement other data sets for a significant model validation.

The only path to approach successfully the problem of morphology distribution in injection molding is to obtain fully characterized sets of data on a material whose behavior is known at the best of current

knowledge in conditions as close as possible to the real processing conditions.

In the following part of this paper, an effort has been made to present a set of data with a complete material characterization, including a thorough study of quiescent crystallization kinetics in a very wide range of cooling rates and a detailed description of the morphology of injection molded samples. The data include all characterization needed for any future investigation. The crystallization kinetics is described with a model able to obtain reliable predictions of material morphology in quiescent conditions in the whole range of cooling rates identified by experimental data (0.01–1000 °C/s). A model describing the evolution of melt morphology is also presented, and implemented in the simulation of the process in order to compare model prediction with experimental results of orientation distribution in the moldings. The phenomenon of flow-induced crystallization is not modeled in the present work, but rather a suggestion for the proper combination between the quiescent morphology and the orientation evolution distribution models is searched from the experimental results of morphology and phase content distribution in the moldings.

2. Material and characterization

A commercial grade iPP resin (T30G; $M_w = 481,000$; $M_n = 75,000$; tacticity $= 87.6\%$mmmm), kindly supplied by Montell (Ferrara, Italy), was adopted for the experiments. Main characterization of the resin adopted are summarized in the following.

2.1. PVT description

Material PVT behavior as a function of temperature, pressure and (overall) crystallinity degree was described as [60]

$$v(T, P) = \chi v_{0\ cr}(1 + \alpha_{cr}(T - T_0) - \beta_{cr}P) \\ + (1 - \chi)v_{0\ am}(1 + \alpha_{am}(T - T_0) - \beta_{am}P) \tag{44}$$

where the reference temperature T_0 was chosen as 298 K, χ is the overall crystallinity degree (keeping into account all crystalline phases), $v_{0\ cr}$ is specific volume of a fully crystalline sample (taken as 1.03 cm³/gr [96] at $T_0 = 298$ K), $v_{0\ am}$ is specific volume of a fully amorphous sample (taken as 1.2 cm³/gr [96] at $T_0 = 298$ K), α is thermal expansion coefficient ($\alpha_{cr} = 0.0002$ K⁻¹, $\alpha_{am} = 0.0006$ K⁻¹), β is compressibility factor ($\beta_{cr} = 9.8 \times 10^{-10}$ l/Pa, $\beta_{am} = 9 \times 10^{-9}$ l/Pa [51]).

The values of α and β were found by a best fit of literature results [97].

2.2. Quiescent crystallization kinetics

Crystallization model described by Titomanlio and co-workers [40] was adopted in this work. This model is able to satisfactorily describe morphological characteristics of samples solidified under quiescent conditions in a very wide range of cooling rates (up to several hundreds of K/s). In particular, the model correctly predicts the presence of two crystalline phases (α and mesomorphic) and an amorphous phase in the solid samples: α-phase prevails on the mesomorphic at low cooling rate (smaller than about 20 K/s at 343 K) and mesomorphic phase prevails on α at higher cooling rates. Since the presence of the two crystalline phases influences morphological characteristics and thus the final properties of the solid, both of them must obviously be taken into account in the modeling of the system.

According to the model, the mesomorphic phase competes with the α form for the available amorphous. Mesomorphic phase is assumed to be isokinetic, and Nakamura kinetic equation (Eq. (4)) was adopted for the expectancy of crystallized volume of mesomorphic phase. A simple Gaussian shaped curve (Eq. (6)) was adopted for the description of the kinetic constant of mesomorphic phase.

Eqs. (2) and (3) were adopted for the description of the two crystallization kinetics.

The evolution of the α crystalline form was described by Kolmogoroff's model (Eq. (9), for three-dimensional growth). Eq. (11) was adopted for the nucleation density (an heterogeneous nucleation was assumed in agreement with experimental observations) and the growth rate $G(T)$ was described by Eq. (10).

Once final values of both crystallinity and number of nuclei have been calculated, the average final radius of the α spherulites, can be calculated by Eqs. (14) and (15).

The model was identified on the basis of a set of data covering a very wide range of crystallization conditions [40]: isotherms covering the temperature range 394–407 K, nucleation density and spherulitic growth rate in the temperature range 394–418 K, cooling rates covering the range 0.01–300 K/s. The values for the parameters of Eqs. (4), (10) and (11) are reported in Table 2.

The model was able to predict the average spherulites radii in samples obtained with very different cooling rates [40].

Table 2
Values of the parameters of crystallization kinetics (Eqs. (4), (10) and (11)) for the iPP considered (Montell T30G)

$N_0 = 17.4 \times 10^{12}$ nuclei/μm^3	$\psi = 0.155$	$K_g = 534{,}858$	$T_m = 467$ K
$G_0 = 2.1 \times 10^{12}$ $\mu m/s$	$T_\infty = 236$ K	$\chi_{eq\alpha} = 0.55$	
$n = 2.83$	$T_{max} = 318$ K	$D = 38.3$ K	
$\chi_{eqmeso} = 0.44$	$U/R = 755$ K	$K_0 = 4.4$ s^{-1}	

Table 3
Values of the parameters adopted to describe the viscosity of iPP T30G by Eqs. (45)–(47)

Parameter	Value	Parameter	Value
A_1	1.74	f_1	3.5×10^{13}
A_2	301.4 K	f_2	11.86
C	0.0023	m	0.17
r	0.34		
B	6387 Pa s		
D_1	503 K		
D_2	0.17 K/bar		

2.3. Viscosity

Shear viscosity curves of the material are well described by the following modified form of the Cross-WLF model:

$$\eta(\gamma\prime, T, P, \chi) = \frac{B\,\alpha(T, P, \chi)}{1 + C\,[B\,\alpha(T, P, \chi)\,\gamma\prime]^{1-r}} \quad (45)$$

where

$$\alpha(T, P, \chi) = 10^{-(A_1(T-D_1-D_2P))/(A_2+T-D_1)} h_\chi(\chi) \quad (46)$$

is a shift factor describing the effect of temperature, pressure and crystallinity.

The values of model parameters are reported in Table 3. The value of 0.17 K/Pa was taken for the parameter D_2, according to literature indications [98].

A comparison between experimental data of melt viscosity, measured both by rotational and capillary rheometry, and model results is reported in Fig. 1.

The description of the effect of (overall) crystallinity degree, χ, on viscosity is also considered in a slightly modified form of Eq. (19), by introducing the multiplying factor

$$h_\chi(\chi) = \left[1 + f_1 \exp\left(-\frac{f_2}{\chi^m}\right)\right] \quad (47)$$

in the expression of the shift factor (Eq. (46)) rather than in the expression of the viscosity itself, as proposed by Titomanlio and co-workers [15]. By adopting this choice, the increase of viscosity by effect of crystallinity become higher at lower shear rates. Such a feature is shown by a recently presented set of data reported on the same material used in this work [62], it regards results of complex viscosity at 431 K after a previous annealing at 411 K during which the material underwent crystallization (this technique was named 'inverse quenching' by the authors). The quiescent crystallization kinetic model described in the previous section was adopted to calculate the crystallinity degree resulting from each annealing time given by Grizzuti et al. [62] and thus complex viscosity curves at 431 K for different crystallinity degrees were obtained and are reported in Fig. 2 as symbols. As shown by the data, by effect of crystallinity on viscosity
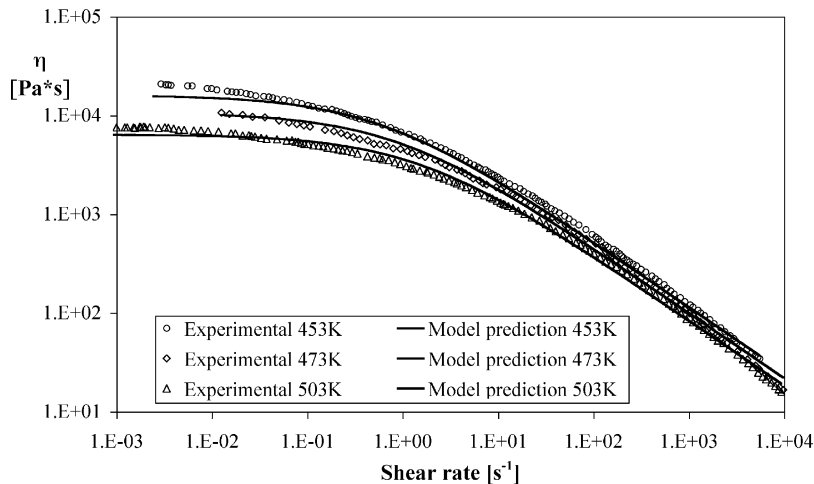

Fig. 1. Experimental data of melt viscosity of iPP T30G, measured both by rotational and capillary rheometry, and model results (Eq. (45), with parameter values listed in Table 3).
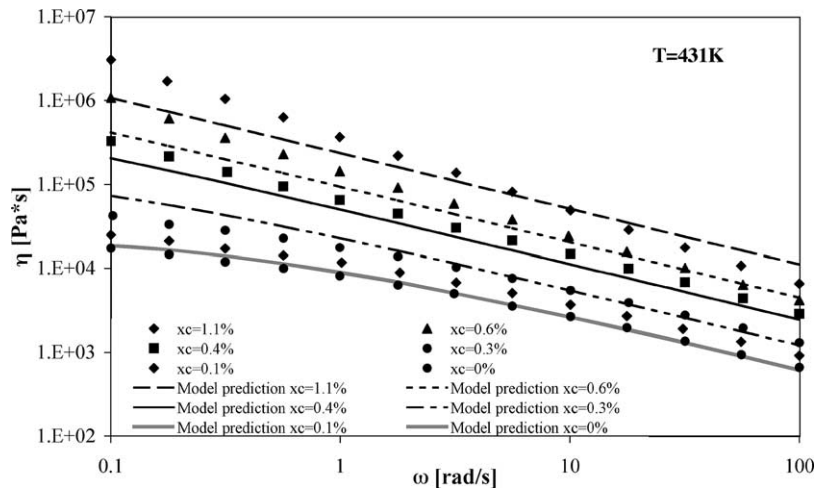
Fig. 2. Effect of crystallinity on viscosity of iPP T30G. Data are taken from Ref. [64], model predictions are calculated by Eqs. (45)–(47) on the basis of parameter values listed in Table 3.

increases by a factor larger at lower shear rates. This feature is captured by Eqs. (46) and (47), whereas Eq. (19) describes the same effect of crystallinity at all shear rates. The values of the parameters of Eq. (47) (f_1, f_2, m) were found by a best fitting on the data reported in Fig. 2, and are reported in Table 3. The results of Eq. (45) are compared with experimental data in Fig. 2.

2.4. Viscoelastic behavior

The non-linear formulation of the elastic dumbbell model described in Section 1.1.5 [20] was adopted in this work to describe the viscoelastic nature of the iPP resin T30G.

Parameters in Eqs. (31) and (32) were determined as a best fitting of data of relaxation time as obtained by oscillatory measurements [76]. In particular, by assuming the validity of Cox–Merz and Laun [99] rules, the relaxation time is obtained as a function of temperature and shear rate as

$$\lambda(T, \dot{\gamma}) = \frac{G'(T, \omega)}{\omega G''(T, \omega)} \left[1 + \left(\frac{G'(T, \omega)}{G''(T, \omega)} \right)^2 \right]^{0.2} \Big|_{\omega = \dot{\gamma}} \tag{48}$$

where G' and G'' are the loss and storage moduli, respectively, and ω is the frequency. The values of the parameters in equations from 31 to 33 where found by a best fitting procedure to the values of relaxation time calculated by Eq. (48) on the basis of results of dynamic measurements.

In particular, data of G' and G'' at constant crystallinity degree were considered [100] in Eq. (48)

in order to obtain the curves of relaxation time as a function of shear rate. The values of the parameters of Eqs. (31) and (32) (with h'_χ set to 1) were determined first, as reported in Table 4, from data at zero crystallinity and at different temperatures.

The values of the parameters in Eq. (33) (e_1, e_2, p) were then obtained by a best fitting procedure on the curves of relaxation time obtained by applying Eq. (48) to the data of Fig. 3, regarding the effect of crystallinity on relaxation time at 158 °C. All the values found are reported in Table 4, and a comparison between results of Eq. (48) (data) and Eq. (31) (model) are reported in Fig. 3 for several crystalline degrees.

3. Injection molding tests and analysis of the moldings

3.1. Injection molding tests and sample preparation

Experiments were performed on a 65-ton Penta injection molding machine equipped with an

Table 4
Values of the parameters adopted to describe the viscoelastic behavior of iPP T30G (Eqs. (31)–(33))

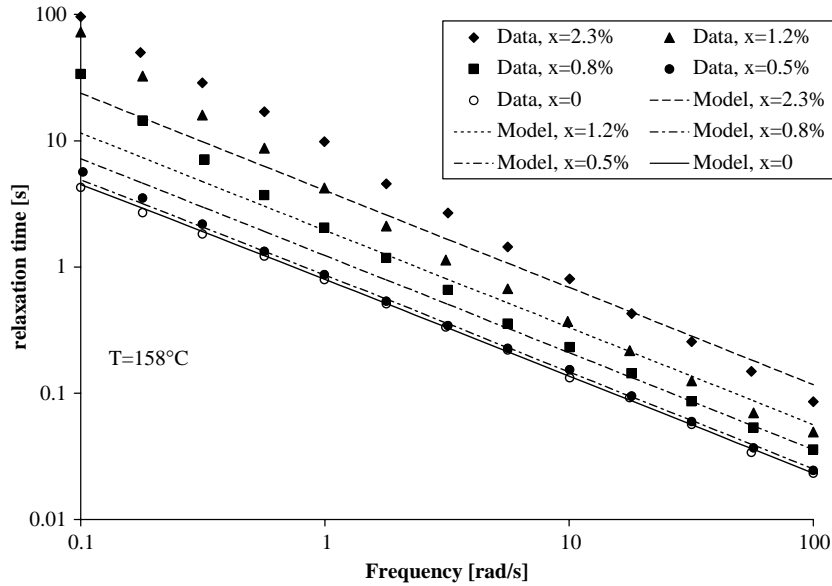| Parameter	Value	Parameter	Value
F_1	2.5	e_1	6.12×10^{13}
F_2	301.4 K	e_2	12.32
E	3.5	p	0.18
b	0.23		
λ^*	14 s		
B_1	503 K		
B_2	0.17 K/bar		

Fig. 3. Effect of crystallinity on relaxation time of iPP T30G. Data are taken from Ref. [64]. Model predictions are calculated by Eqs. (31)–(33) with the values of parameters listed in Table 4.

instrumented mold. A nozzle of diameter 2.2 mm and length 40 mm was adopted. The sprue tapered from a diameter of 7 mm to a diameter of 4.7 mm over a length of 80 mm. The runner had a diameter of 8 mm and was 68 mm long. The material was injected into a line gated rectangular cavity of $120 \times 30 \times 2$ mm^3. Five Kistler piezoelectric pressure transducers were mounted along the flow path. In particular, one transducer was mounted in the injection chamber, one in the runner and the others in the cavity (15, 60 and 105 mm downstream to the gate). These positions will be referred to as P0, P1, P2, P3 and P4, respectively. A complete description of mold geometry is reported

elsewhere [24]. Transducers signals were read by a data acquisition system and stored in a computer.

For crystallinity and morphology investigations, thin slices were cut by means of a Leica slit microtome from molded samples at the cavity positions where pressure transducers were located. Details of cutting procedures are illustrated in Fig. 4: first, a molded sample was cut into three blocks in correspondence of pressure transducers positions (15, 60, 105 mm from the gate), then thin slices (about 25 μm thick) were cut from the central part of each block along flow (x) direction and parallel either to the flow-thickness (x, y) plane (scheme A in Fig. 4) or to the flow-width (x, z) plane (scheme B
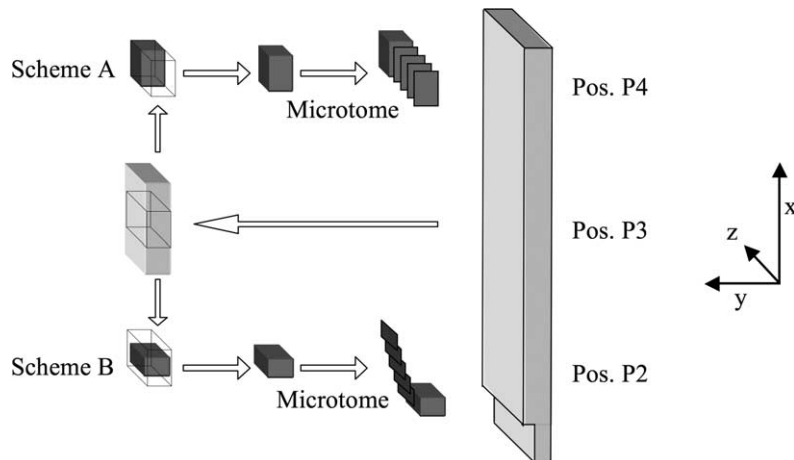
Fig. 4. Cutting procedures followed to obtain the slices for microscopy.

in Fig. 4). Slices cut according to scheme A refer therefore to a full thickness (2 mm) section of the sample in the considered position (P2/P3/P4) and at 15 mm from sample lateral edge. Vice versa, slices cut according to scheme B refer to sections at different distances from sample skin. All slices were cold lapped soon after cutting procedure.

3.2. Microscopy

3.2.1. Optical microscopy

In order to gather information on morphology changes with distance from the sample skin, thin slices, cut from injected samples according to scheme A (flow-thickness plane) in P2, P3 and P4, were analyzed by polarized light optical microscopy.

3.2.2. SEM and AFM analysis

In order to better characterize morphological distribution in injection molded samples, slices already observed by means of optical microscopy, were chemically etched according to the procedure suggested by Bassett [101] and then observed using both scanning electronic microscopy and atomic force microscopy. The etchant used was a solution of potassium permanganate in a mixture of 10:4:1 volumes of concentrated sulphuric acid, orthophosphoric acid and distilled water, respectively (1 g of potassium permanganate in 100 ml of mixture). A 2-h period of etching at room temperature was generally sufficient to reveal the surface topography.

A Leo-420 (Assing) scanning electron microscope was used at an accelerating voltage of 10 kV. Prior to microscopy examination, the surfaces of the samples were coated with a thin layer of gold by ion sputtering.

TM-AFM data were acquired in ambient with a NanoScope III multimode AFM (Digital Instruments (DI), Santa Barbara, CA) using micro fabricated silicon tips/cantilevers. Height (constant amplitude damping), amplitude (error signal), and phase images were recorded simultaneously. In the simplest AFM modes of operation (contact and 'tapping'), topographic images representing the surface of the polymer specimen can be obtained, with a resolution which are beyond that achievable with SEM imaging of polymers [102].

3.3. Distribution of crystallinity

3.3.1. IR analysis

Slices microtomed from injected samples parallel to the sample skin (Scheme B) were analyzed by means of an IR spectrophotometer (Brucker device), measuring the absorbance in the range 400–4000 cm^{-1}.

The crystallinity degree distribution was determined by the analysis of the FTIR absorbance spectra applying Lambert and Beer's law to selected peaks. Considering a crystalline and an amorphous peak and assuming that the absorbance of both the amorphous and the crystalline phases do not depend on phase-content distribution, Lambert and Beer's law provides, respectively

$$A_{cr} = a_{cr}S\xi \tag{49}$$

$$A_{am} = a_{am}S(1-\xi) \tag{50}$$

where A_{cr} and A_{am} are the absorbancies; a_{cr} and a_{am} are the absorption coefficients of the crystalline and amorphous phases peak, respectively; ξ is the crystallinity degree and S is the sample thickness.

The value of ξ may be obtained by eliminating S from Eqs. (49) and (50):

$$\xi = \frac{A_{cr}}{A_{cr} + (a_{cr}/a_{am})A_{am}} \tag{51}$$

The value of ξ, can thus be calculated from measurements of absorbance if the ratio of absorptivities is known. This parameter is normally estimated using an independent experimental technique.

Several absorption bands of the crystalline fraction have been identified. The most defined and isolated one is at 841 cm^{-1} due to CH_2 rocking and CH axial bending. Another band partially overlapping the first one is the band at 998 cm^{-1}, due to CH_3 equatorial rocking, C–CH_3 stretching, CH bending and CH_2 twisting. All the mentioned bands are sensitive to the order of long helical chains, and then they measure the contribution to order of α phase as well as of β phase and of mesomorphic structures. Thus crystallinity degree as measured by IR is an average crystallinity degree: it is not possible to discriminate contributes of different phases. As for the amorphous phase bands, the peaks at 973 cm^{-1} is the most commonly adopted [103]. In this work, the band at 841 cm^{-1} was chosen for crystalline phase and the band 973 cm^{-1} for amorphous phase. The ratio of absorptivities was calculated as 0.58 by calibration with density measurements. Because the spectra are the weighted superposition of single absorption peaks, all the absorbencies were obtained by fitting the experimental spectra with a weighted combination of single peaks, adopting Gaussian/Lorentzian peak functions.

3.3.2. X-ray analysis

As mentioned above, FTIR analysis does not allow to discriminate between different crystalline phases and thus the crystallinity degree as measured by FTIR analysis has to be considered as an overall value accounting for all existing crystalline phases. Thus in order to discriminate between different crystalline phases some thin slices cut from the moldings according to the scheme B were analyzed using WAXD.

Two-dimensional WAXD patterns can be circularly averaged to generate plots of diffracted intensity as a function of angle 2θ. WAXD patterns were analyzed by a deconvolution procedure performed according to a scheme reported in the literature [104] and summarized below. The full spectrum is considered as a super-position of the a number of reflections, due to each phase present (12 reflections were considered: 7 for the α phase, corresponding to $2\theta = 14.1$, 16.9, 18.6, 21.2, 22.1, 25.5 and 28.5; 2 for the mesomorphic form, corresponding to $2\theta = 14.5$ and 21; 2 for the β form, corresponding to $2\theta = 16$ and 21; 1 for the amorphous halo); each reflection being described by a combination of a Lorentzian function and a Gaussian function.

The parameters defining each reflection were determined, with a general purpose optimization routine, adopting as objective function the total quadratic error with respect to the experimental spectrum.

The content of each phase in the samples was then calculated as

$$\xi_i = \frac{A_i}{\sum_i A_i} \tag{52}$$

where A_i are the areas under selected peaks.

Obviously, deconvolution results are affected by some uncertainty, it was estimated as $\pm 3\%$ on the percentage of each phase.

3.4. Distribution of molecular orientation

IR spectroscopy is a very useful technique also for the assessment of chain orientation. According to the hypothesis of uniaxial orientation the orientation parameter (Hermann's factor) can be evaluated as [103]

$$f = \frac{3\langle\cos^2\vartheta\rangle - 1}{2} = \frac{(D_r - 1)(D_{r0} + 2)}{(D_r + 2)(D_{r0} - 1)} \tag{53}$$

where D_r is the dichroic ratio, namely the ratio between the absorbance of the infrared radiations polarized along directions parallel and perpendicular to the direction of orientation.

There are some infrared absorption bands that are characterized by absorption in both the crystalline and the amorphous phases. The 1256 cm^{-1} band of isotactic polypropylene is such a 'mixed' band, and is considered in this work as indicative of an average orientation. In fact, since this band results from the absorption in both the crystalline and the amorphous regions, its infrared dichroism would be expected to correlate with some average orientation function ($\alpha_\nu = 38.5°$, $D_{r0} = 3.1610$). Also in this case a deconvolution technique was applied to identify the absorbance at 1256 cm^{-1}.

Measurements of light intensity were performed with a polarizing microscope downstream to the crossed analyzer as function of the angle of the sample cut according to scheme A, the minimum of this intensity identifies the direction of orientation. Measuring spots of about 100 mm in diameter were adopted and measurements were performed moving the objective from the skin to the sample midplane.

4. Analysis of experimental results

4.1. Injection molding tests

The injection molding experiments (three series) were carried out under different molding conditions, as listed in Table 5, and allow to underline the effects of injection speed and mold temperature on both crystallinity and microstructure distribution in the moldings.

-In the first series, nominal injection flow rate was 15 cm^3/s, holding pressure was 400 bar, holding time was 10 s, melt injection temperature was 503 K and mold temperature was 303 K. These molding conditions were considered as 'standard' conditions, and this sample was used as a reference in order to evaluate the effects of operative conditions on the crystallinity and microstructure distribution inside the moldings; in the second series, in order to study flow rate effects, a different nominal injection flow rate was applied (5 cm^3/s), all other variables were left unchanged with respect to 'standard' conditions; in the third series, in order to study mold

Table 5

Processing parameters and 'code' of the three series of molding experiments performed in this work

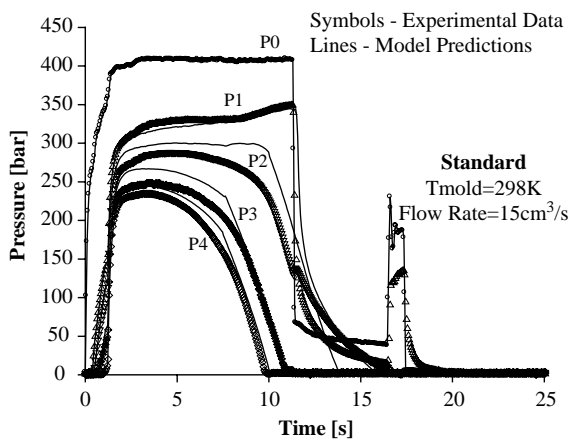|	Standard sample	Slow sample	High T sample
Flow rate (cm^3/s)	15	5	15
Mold temperature (K)	303	303	343
Holding pressure (bar)	400	400	400
Holding time (s)	10	10	15

Fig. 5. Experimental and simulated pressure curves for 'standard' sample. P0–P4 indicate the position of pressure transducers: P0 in the injection chamber; P1 in the runner, just upstream to the gate; P2 inside the cavity, 15 mm from the gate; P3 inside the cavity, 60 mm from the gate; P4 inside the cavity, 105 mm from the gate. Lines refer to model predictions (Section 5.1).

temperature effects, a different mold temperature was applied (343 K) and also in this case all other variables were left unchanged with respect to 'standard' conditions.

Experimental pressure evolution curves in the five transducers positions are reported in Figs. 5 and 6 for all tests.

Injection molding cycle can be divided into three distinct stages. In the first stage the mold fills up with polymer and there is a moderate increase in pressure. Once the mold is full, the second stage begins and pressure is increased drastically so that additional material is packed into the mold to compensate for shrinkage caused by the increase of density of with subsequent temperature decrease and crystallization. Finally, after gate freezing, the cooling starts and there

is a progressive pressure reduction. The effects of various process parameters such as flow rate (injection speed) and mold temperature on pressure traces during the filling and packing stages can be also evaluated from Figs. 5 and 6. For instance, the effect of a higher mold temperature is clear by comparing 'high T' test (Fig. 6, right) with 'standard' test (Fig. 5): due to a much slower cooling, and being the viscosity lower, pressures reach higher values and remain higher for a much longer time in all positions inside the cavity.

4.2. Morphology distribution along thickness direction

4.2.1. Optical microscopy

Micrographs in cross-polarized optical light of slices cut along the flow-thickness plane (Scheme A of Fig. 4) in position P3 (central in cavity) from all moldings analyzed in this work are reported in Fig. 7. Two series of micrographs are reported: in the first one, Fig. 7a, the slices are oriented so that the flow direction is aligned along polarizer direction; in the second one, Fig. 7 b, the slices are rotated of 45°. Normally, the change of brightness during a 45° rotation is directly proportional to the material orientation level. Micrographs reveal a morphology distribution typical of an injection molded semi-crystalline sample, often referred to as skin–core morphology, characterized by the presence of a series of distinct regions: a thin, oriented skin layer (of the order of 10 μm); an oriented non-spherulitic zone (often referred as 'shear layer', the dark zone in Fig. 7 a); a spherulitic core with essentially no preferred orientation. The thickness of the oriented region including both the skin layer and the shear zone (referred to in the following as 'dark zone') is denoted as δ in the following.
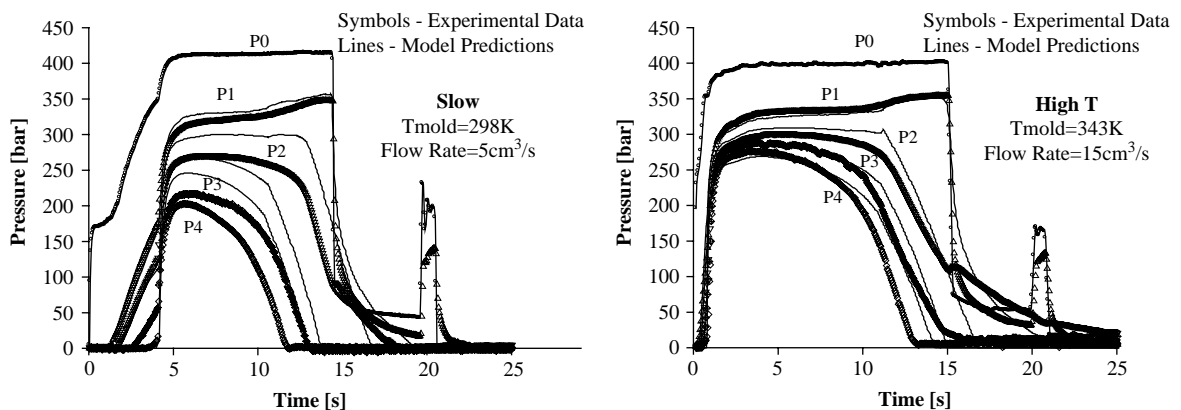

Fig. 6. Experimental and simulated pressure curves for 'slow' and 'high T' samples, respectively. P0–P4 indicate the position of pressure transducers: P0 in the injection chamber; P1 in the runner, just upstream to the gate; P2 inside the cavity, 15 mm from the gate; P3 inside the cavity, 60 mm from the gate; P4 inside the cavity, 105 mm from the gate. Lines refer to model predictions (Section 5.1).
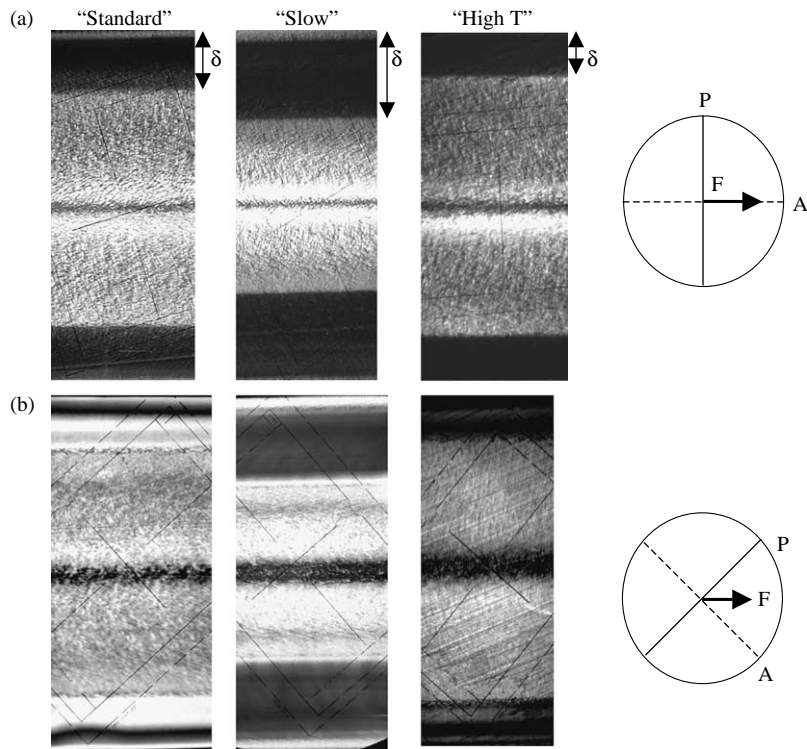
Fig. 7. Optical micrographs in position P3. The alignment of the samples between crossed polarizers is reported on the right: 'A' represents the analyzer; 'P' represents the polarizer; 'F' represents the flow direction.

The effect of process parameters on the shear layer thickness of the moldings is clearly shown in Fig. 7: consistently with literature indication [43], the thickness of the shear layer shown by the 'slow' sample is larger than the ones of the other samples; furthermore, it can easily be noticed that δ decreases on increasing injection temperature.

4.2.2. SEM and AFM analysis

In order to better characterize the skin–core morphology, the same slices analyzed by optical microscopy and shown in Fig. 7 were chemically etched according to the procedure described in Section 3.2, and then observed using scanning electronic microscopy and atomic force microscopy.
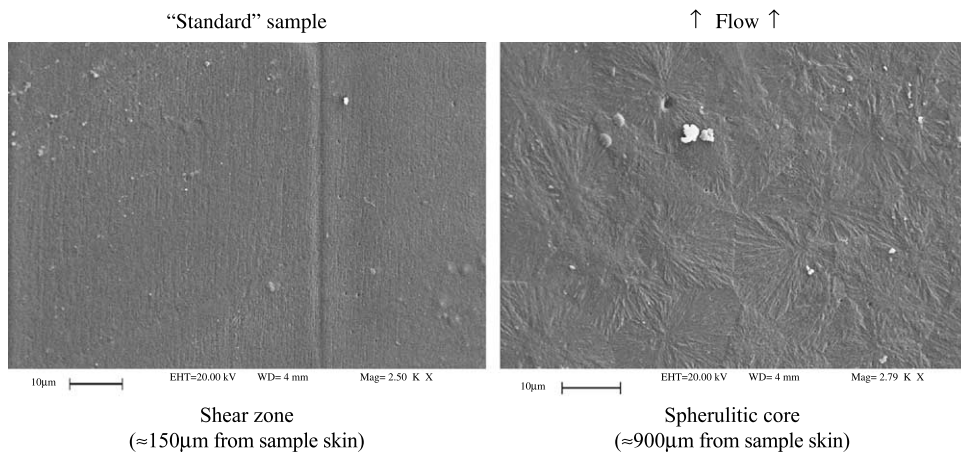
Fig. 8. SEM micrographs of 'Standard' sample in position P3. Internal layers, on the right, are fully spherulitic; inside of the shear zone, left, highly oriented structures (fibrils) are observed.

"Slow" sample ↑ Flow ↑

Shear zone
(≈350μm from sample skin)

Spherulitic core
(≈900μm from sample skin)
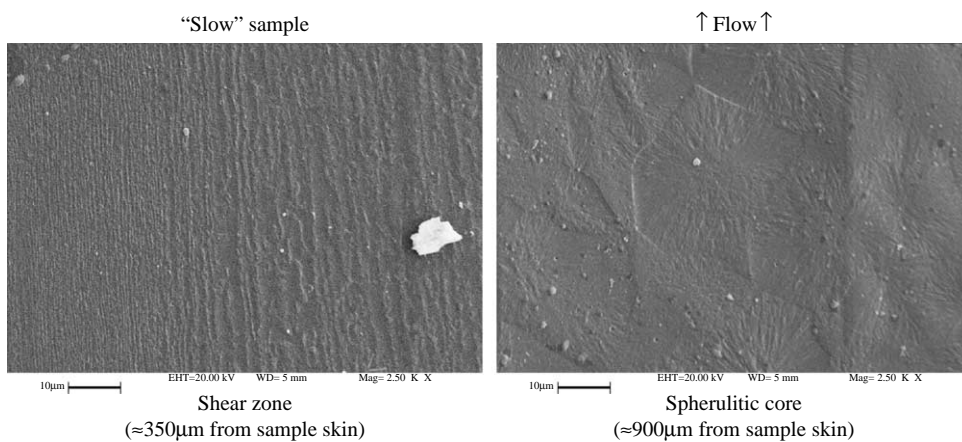
Fig. 9. SEM micrographs of 'Slow' sample in position P3. Internal layers, on the right, are fully spherulitic; inside of the shear zone, left, highly oriented structures (fibrils) are observed.

"High T" sample ↑ Flow ↑

Shear zone
(≈150μm from sample skin)

Spherulitic core
(≈900μm from sample skin)
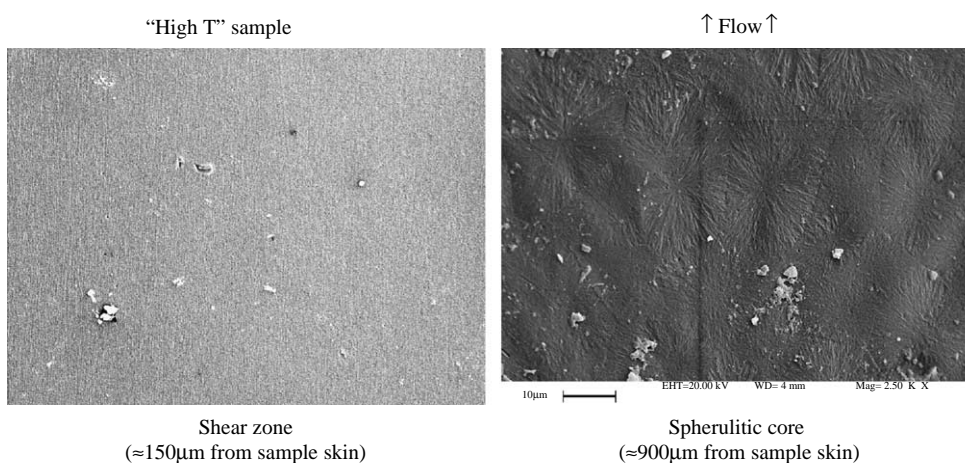
Fig. 10. SEM micrographs of 'High T' sample in position P3. Internal layers, on the right, are fully spherulitic; inside of the shear zone, left, highly oriented structures (fibrils) are observed.

"Standard" sample ↑ Flow ↑

Spherulitic core
(≈900μm from sample skin)

Spherulitic core
(≈900μm from sample skin)
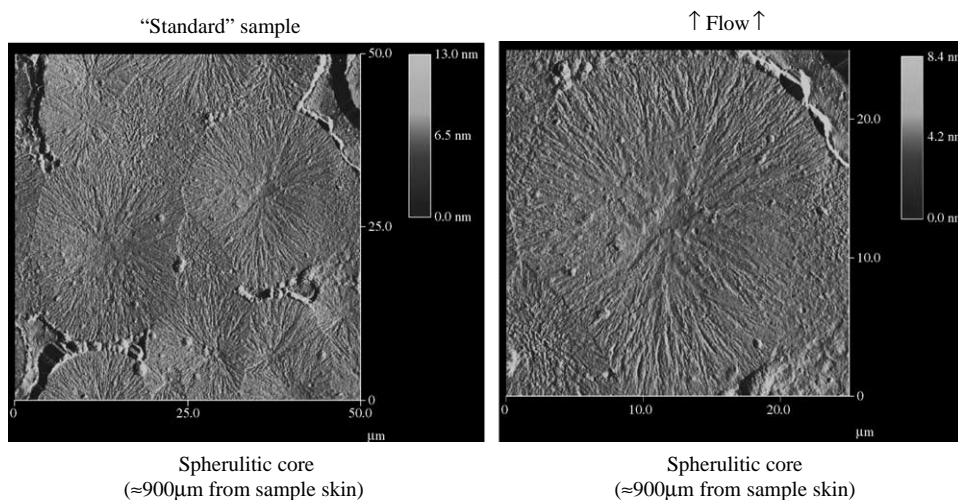
Fig. 11. AFM images of the spherulitic core of 'standard' sample in position P3.

"Standard" sample   ↑ Flow ↑

Dark zone of figure 7a   Dark zone of figure 7a
(≈100μm from sample skin)   (≈350μm from sample skin)
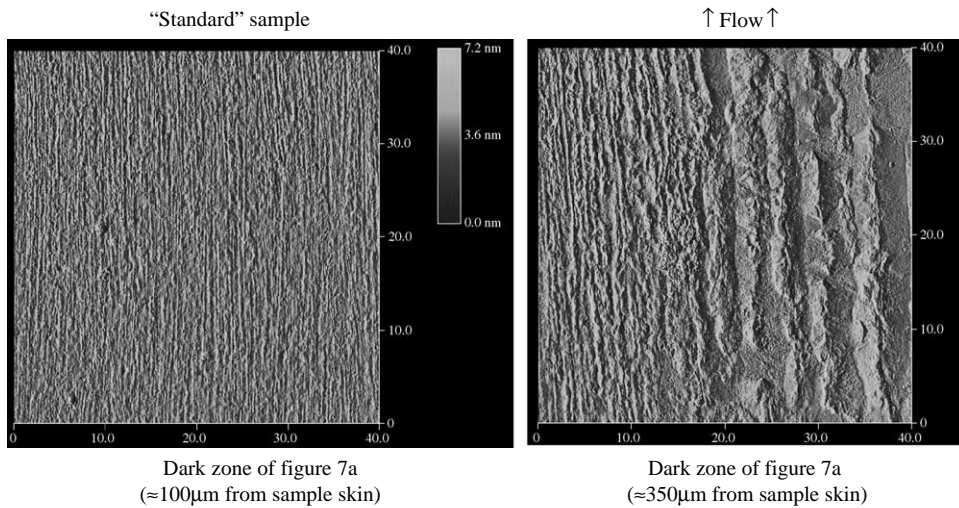
Fig. 12. AFM images in shear zone ('Standard' sample, position P3).

SEM micrographs are reported in Fig. 8 ('standard' sample), Fig. 9 ('slow' sample), and Fig. 10 ('high T' sample): within each figure, the first micrograph refers to the shear zone and the second one to the central layer (sample midplane). SEM observations confirm results obtained by optical microscopy for all samples analyzed: internal layers resulted to be fully spherulitic whereas inside of the shear zone highly oriented structures (fibrils) were observed.

AFM analysis confirms results obtained by SEM for all samples analyzed: internal layers resulted to be fully spherulitic, whereas inside of the shear zone highly oriented structures (fibrils) were observed.

AFM micrographs only of standard sample are reported in Figs. 11–13. Similar results were also obtained for the 'fast' and 'high T' samples. The morphologies of the core, the shear layer and the transition between them can be observed in Figs. 11 and 12.

Further details can be captured from the three-dimensional image of the etched shear zone reported in Fig. 13. A careful analysis of micrographs showed that the distance between the fibrils in the shear zone
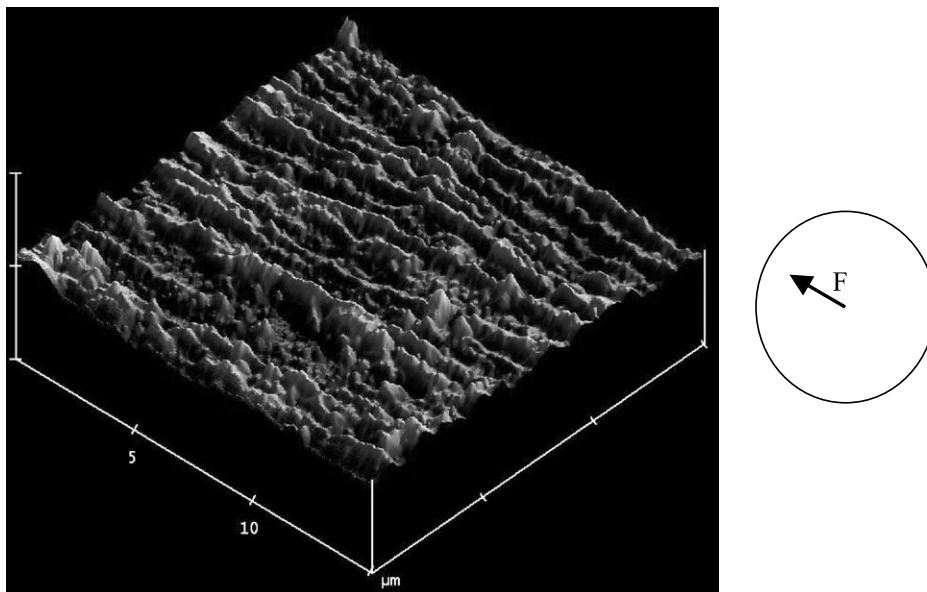
Fig. 13. Three-dimensional image of the fibers (AFM) of 'Standard' sample in position P3.
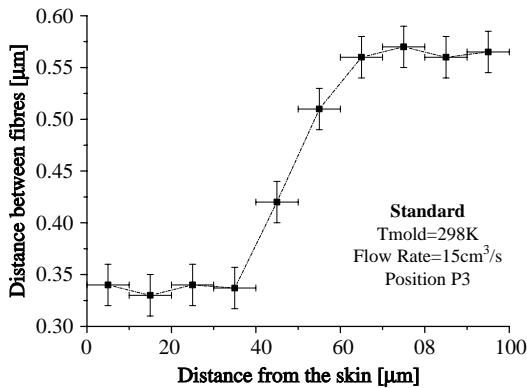
Fig. 14. Distance between fibrils in the 'Standard' sample in position P3 (as measured by AFM analysis), up to 100 μm from the skin.
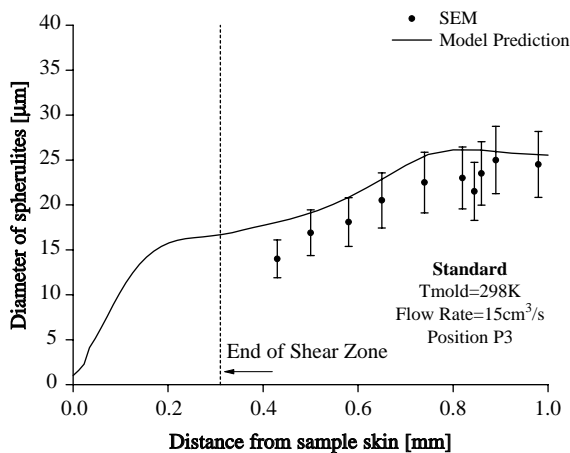

Fig. 15. Average spherulites diameter distribution along thickness in position P3 for the 'standard' sample. Lines refer to model predictions (Section 5.2).
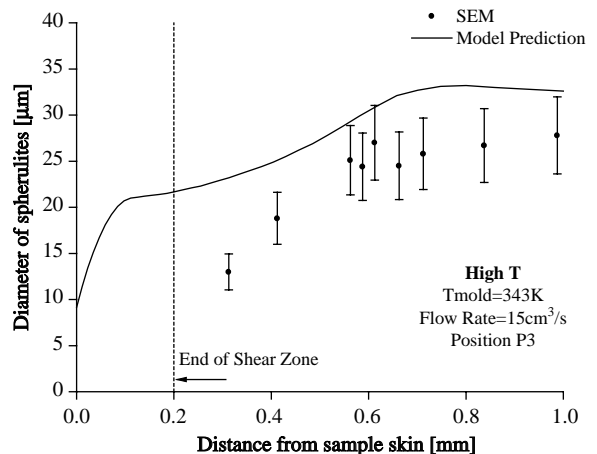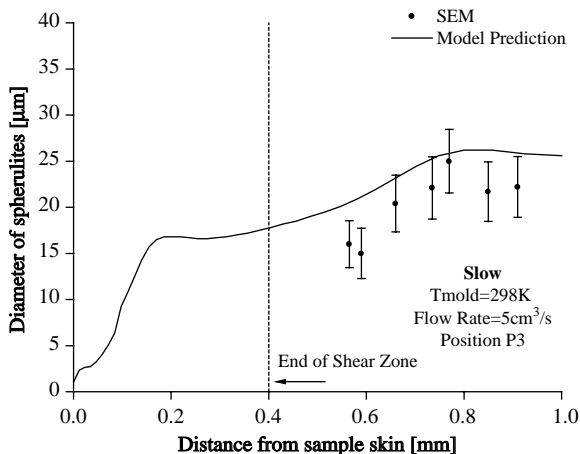
changes with the distance from the sample skin: it is very small near the skin and it increases on increasing the distance from the skin until spherulites replace fibers.

The distribution of the distance between the fibrils inside the highly oriented zone as obtained from AFM micrographs for the 'standard' sample in P3 are reported in Fig. 14.

Currently, little is known concerning the influence of injection molding conditions on spherulite sizes in the core region of injection moldings [43]. Micrographs (obtained by SEM and AFM) were used to evaluate distribution of spherulites diameter along thickness in position central in cavity, P2: diameters of spherulites versus distance from the skin are reported in Figs. 15 and 16.

Figs. 15 and 16 show that the largest spherulites are in the core region and become smaller and smaller from the core region toward the shear zone. Data indicate in the intermediate zone, the 'high T' samples show the biggest spherulites. Moreover, in the 'high T' samples, the shear region is thinner and thus spherulites could be detected in layers closer to the mold wall with respect to all the other samples.

4.3. Morphology distribution along flow direction

Micrographs in cross-polarized optical light of slices cut along the flow-thickness plane (Scheme A of Fig. 4) at all transducer positions inside the cavity for all samples analyzed in this work are reported in Figs. 17–19.

Using the optical microscope, the thickness of the oriented region (skin layer and shear zone) $\delta(x)$, was measured as a function of the distance from the gate, x;
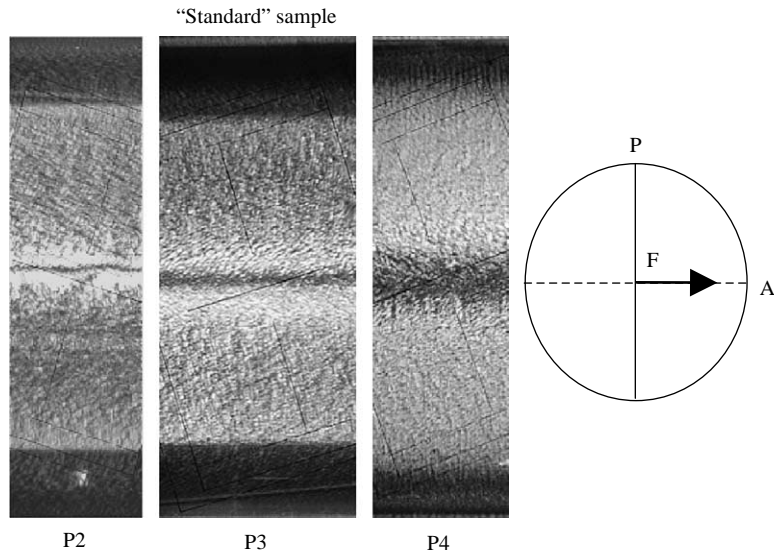

Fig. 16. Average spherulites diameter distribution along thickness in position P3 for 'slow' and 'high T' samples. Lines refer to model predictions (Section 5.2).

"Standard" sample

Fig. 17. Micrographs in polarized optical light of 'Standard' sample along flow direction.

results are reported in Fig. 20 for the three molding conditions considered in this work.

Consistently with literature indications [6,43], the thickness of the shear zone increases with the distance from the gate, goes through the maximum at the intermediate x-location, and then decreases towards the cavity end. Titomanlio et al. also observed that the dark band was not present in sections near the cavity tip [6].

The effect of molding conditions on $\delta(x)$ can be determined: δ is larger for the lowest injection speed. A lower injection speed allows in fact the molten polymer to experience a longer shearing time during the filling stage. On the other hand, a longer shearing time allows the melt to be cooled more effectively during the filling stage. The latter effect results in a low temperature shear also of layers at larger distance from the mold wall. Consequently, as the injection speed decreases, high molecular deformation which for a given shear rate is more effective at low temperature is achieved and highly oriented crystallite microstructure develops on a thicker layer.

Micrographs (obtained by SEM and AFM) were used to evaluate distribution of spherulites diameter along flow direction in the 'standard' sample: in agreement with the literature, a negligible variation in the spherulite sizes along the flow direction was observed [43,105].
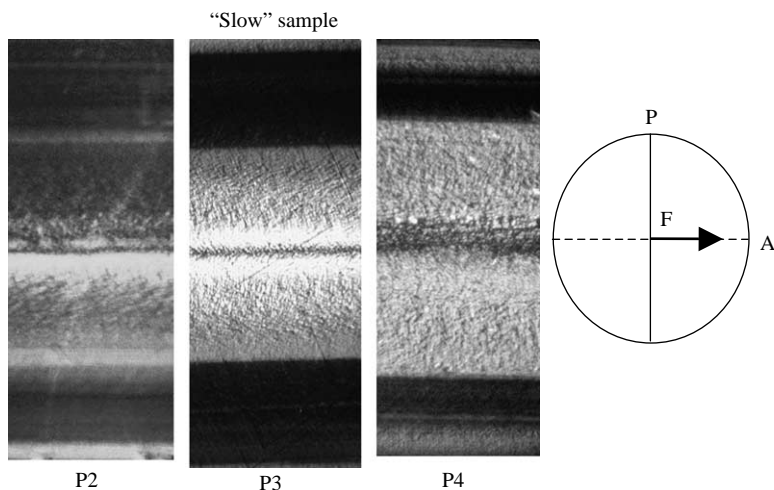
"Slow" sample

Fig. 18. Micrographs in polarized optical light of 'Slow' sample along flow direction.

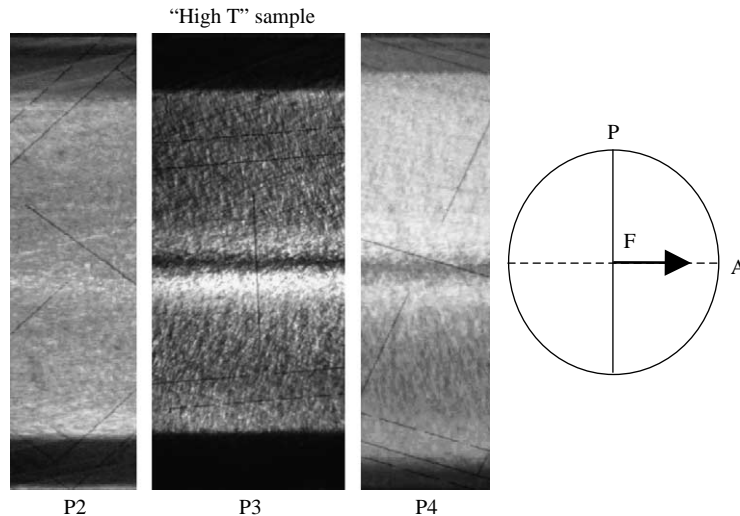"High T" sample

P2   P3   P4

Fig. 19. Micrographs in polarized optical light of 'High T' sample along flow direction.

4.4. Distribution of crystallinity

4.4.1. Distribution of crystallinity along thickness direction

4.4.1.1. IR analysis. Results of crystallinity distribution along thickness in pos P3 (central position in cavity) obtained by means of IR analysis (Eq. (51)) are reported in Figs. 21 and 22. Surprisingly, they show that the final average crystallinity degree is about constant along thickness for all molding tests carried out, in spite of the very high cooling rates experienced during crystallization by the polymer close to sample skin (several hundreds of Kelvin degrees for second), at least for the 'standard' and the 'slow' test.

4.4.1.2. X-ray analysis. As mentioned above, crystallinity degree measured by IR is an average between different crystalline phases. Some of the thin slices cut
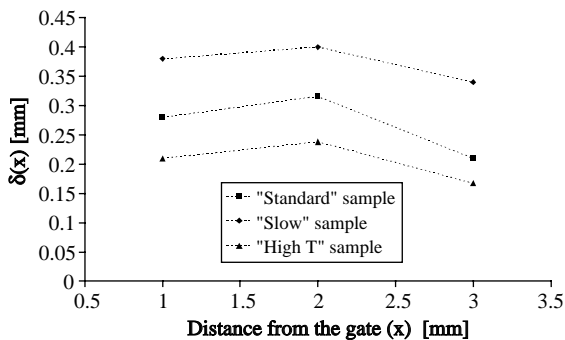
according to scheme B (flow-width plane) in P3 were analyzed by WAXD. Some WAXD patterns are reported in Fig. 23 for all samples analyzed in this work.

In Fig. 23 a and e, a weak near-isotropic ring is observed for the 110 peak; it reveals a fraction of crystallites that are not highly oriented, in spite of the very high stress experienced by the polymer close to sample skin.

Diffraction patterns reported in Fig. 23 b, f, g, i and l correspond to the position of the shear zone: they are characteristic of the monoclinic crystalline unit cell of the α-phase and have a bimodal character. This distinctive pattern is unique to isotactic polypropylene and is attributed to the crystallographic branching of 'daughter' lamellae growing epitaxially

Fig. 20. Skin layer thickness, $\delta(x)$, as a function of the distance from the gate, x.
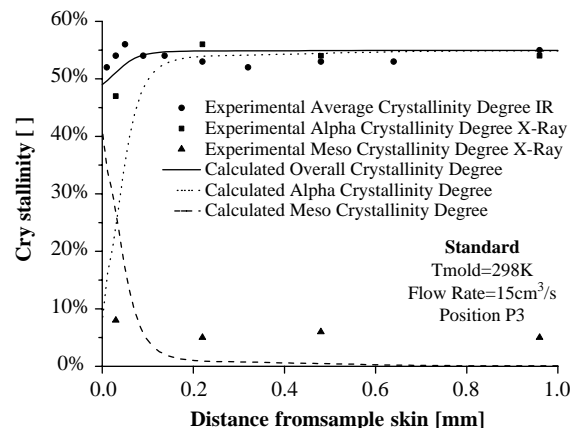

Fig. 21. Crystallinity distribution along thickness obtained by means of IR and X-ray (Section 4.4) analysis in position P3 for the 'standard' sample. Lines refer to model predictions (Section 5.4).
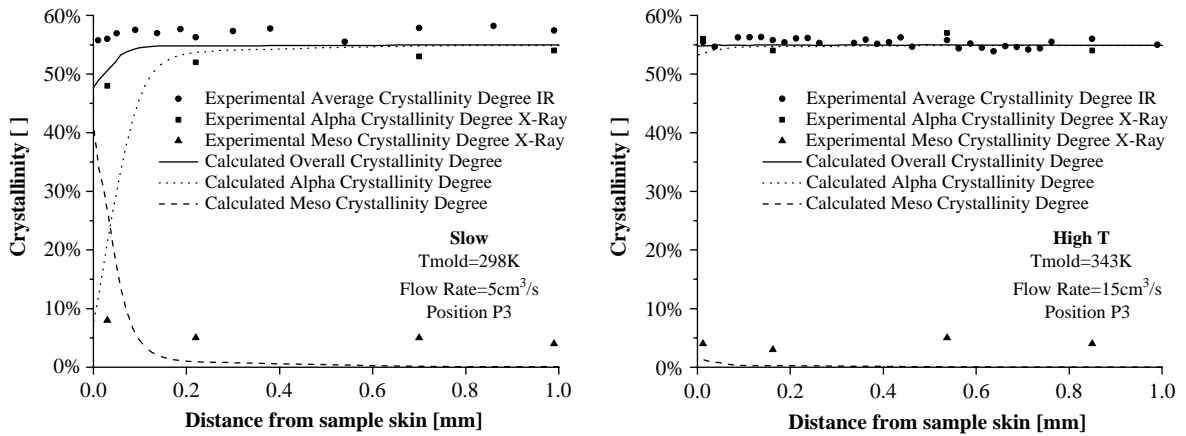
Fig. 22. Crystallinity distribution along thickness obtained by means of IR and X-ray (Section 3.3) analysis in position P3 for the 'slow' and the 'high T' samples. Lines refer to model predictions (Section 5.4).

with their *a*- and *c*-axes parallel to the *c*- and *a*-axes of the 'parent' lamellae, respectively. The diffraction patterns in Fig. 23 b, f, g, i, and l may be interpreted in view of the uniaxial symmetry shown by AFM and SEM micrographs, and can be explained in terms of parent lamellae that have their chain (*c*) axis aligned along the flow direction with a uniaxial distribution about that direction and the *b* axes of parent and
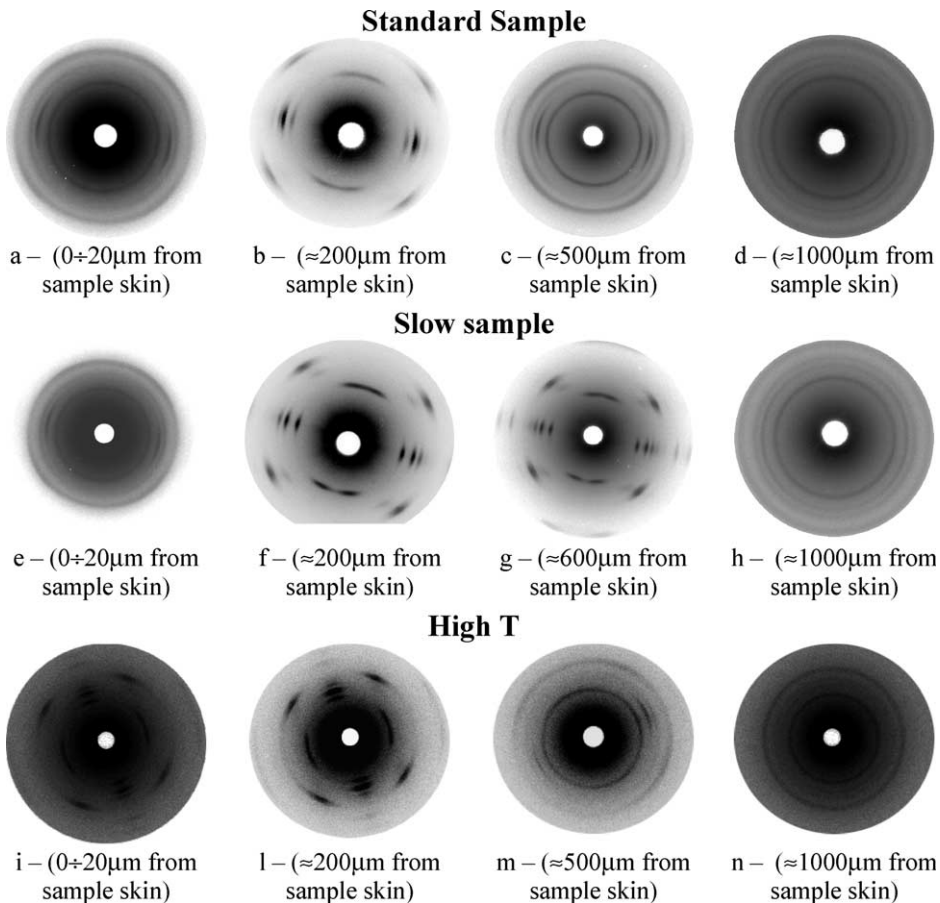

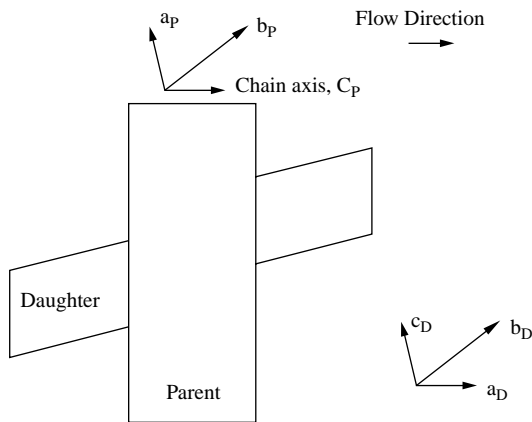Fig. 23. Two-dimensional WAXS patterns for all samples analyzed.

Fig. 24. A schematic model for the alignment of the parent and daughter lamellae in the oriented crystallites that explains the diffraction patterns in Fig. 23b, f, g, i and l.

Fig. 25. X-rays diffractograms of slices microtomed from 'Standard' sample.

daughter lamellae parallel (see Fig. 24) [106]. Similar diffraction patterns were also reported by Mendoza et al. [10].

Two-dimensional WAXD patterns (such as those in Fig. 23) can be circularly averaged to generate plots of diffracted intensity as a function of angle 2θ, resulting patterns are reported in Fig. 25 for 'standard' sample, and in Fig. 26 for 'slow' and 'high T' samples. Diffractograms show the main peaks at 14.1, 16.8, 18.6 and 22° of 2θ (dotted line in figures), characteristic of the monoclinic α form for all slices analyzed.

WAXD patterns were analyzed by a deconvolution procedure performed according to the scheme described in Section 3.3. Results of the deconvolution technique are reported in Figs. 21 and 22 and show that the average crystallinity in the samples appears to be essentially in the α monoclinic form also close to sample skin. It has been suggested in the literature that the imposition of shear on isotactic polypropylene leads to an increased tendency to form the β crystal phase [8,9]. Typical levels of β crystallites in injection molded parts are less than 5% [8] and indeed in our experiments, the percentage of the β phase does not exceed 3%. Furthermore, we did not observe scattering from the γ-phase.

4.4.2. Crystallinity distribution along flow direction
4.4.2.1. IR analysis.
In order to analyze crystallinity degree distribution along flow, IR analysis was performed on slices cut according to scheme B also in positions P2 and P4 (15 and 105 mm from the gate). Results of crystallinity distribution along thickness obtained by means of IR analysis in positions P2 and P4
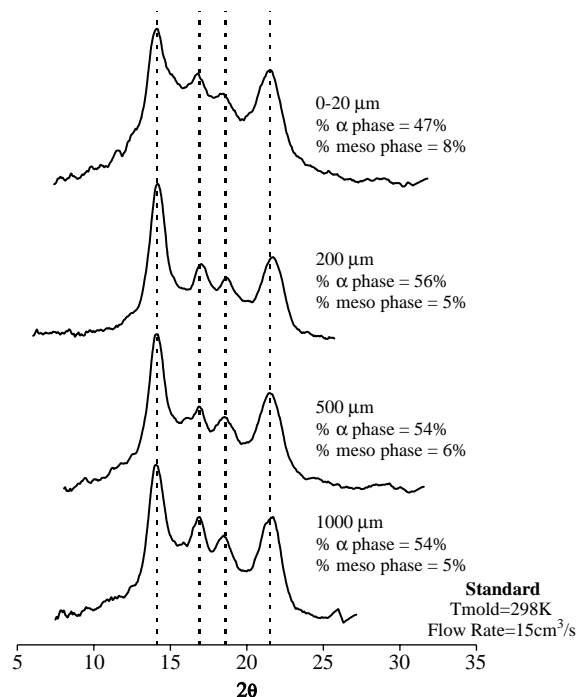
together with results obtained in P3 (60 mm from the gate) allow to gather a complete characterization of crystallinity distribution in the whole sample. Results confirm that the final average crystallinity degree is about constant along thickness in the whole sample for all molding tests.

4.4.2.2. X-ray analysis.
Some of the thin slices cut according to scheme B (flow-width plane) in positions coded as P2 and P4 (15 and 105 cm downstream from the gate) in the 'standard' sample were analyzed by X-rays. WAXD patterns show a behavior similar to that observed in P3 for all molding conditions considered.

4.5. Distribution of molecular orientation

4.5.1. Orientation along thickness direction
Results for the mixed amorphous-crystalline orientation obtained by means of IR analysis (Eq. (53)), performed on slices cut according to scheme B in position P3 are reported in Figs. 27 and 28 and they confirm a highly oriented zone in correspondence of the dark zone of Fig. 7 a with a maximum located at different distances from the skin, depending on molding conditions. In position P3, the molecular orientation essentially decreases on increasing the distance from
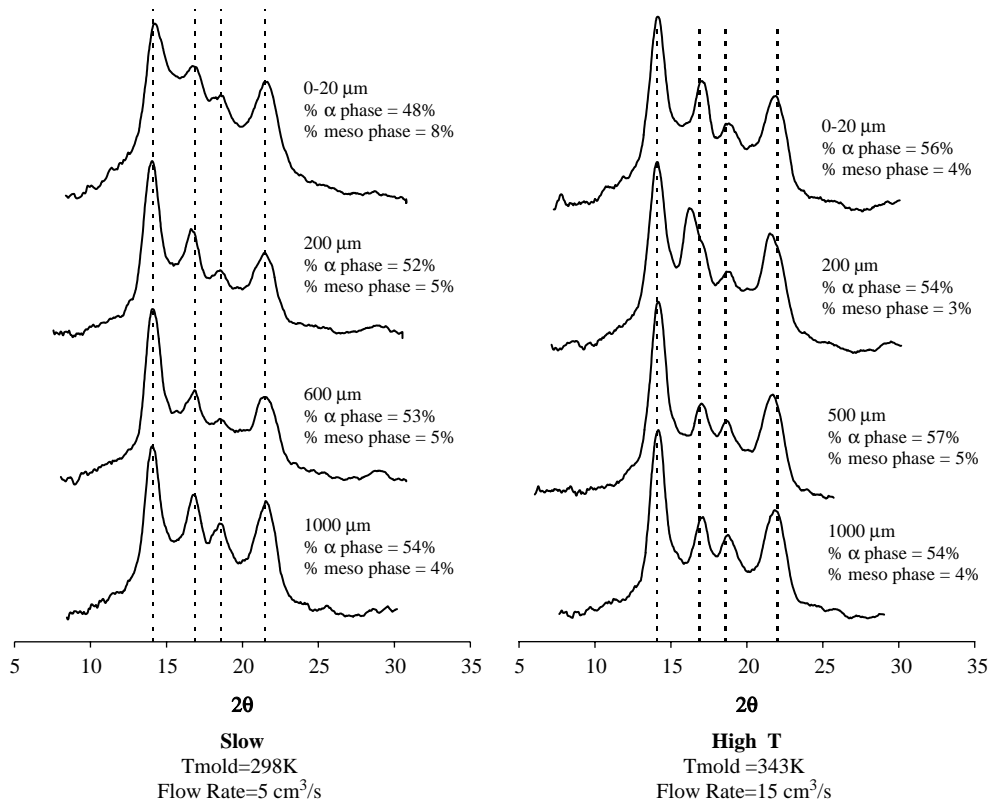
Fig. 26. X-rays diffractograms of slices microtomed from 'Slow' and 'High T' samples.

the skin until the central zone is reached, where no preferred orientation is present. Figs. 27 and 28 show that in the 'slow' sample molecular orientation is certainly higher beyond the shear zone. This happens because, due to the higher filling time, the packing flow takes place at lower melt temperature, and thus it is much more effective in orienting the molecules which have higher relaxation times.

4.5.2. Orientation along flow direction

In order to analyze molecular orientation along flow path, IR analysis was performed on slices cut according to scheme B also in positions P2 and P4 (1.5 and 10.5 cm from the gate). Results are reported in Fig. 29 for 'standard' sample, and results obtained in P3 (60 mm from the gate) are also reported in the same figure for comparison.

Data show that the orientation parameter, calculated by means of IR analysis, decreases on increasing distance from the gate. Also in positions P2 and P4 the highest values are reached in correspondence of the shear zone, but in position P2 orientation remains on high values in the whole thickness; even a second

maximum at about 0.6 mm from skin is observed in position P2, whilst in P3 and P4 after the maximum a constant decrease of molecular orientation takes place. This maximum is normally associated to the effect of packing flow [20], which is absent at the tip of the cavity (position P4) and obviously grows up going backwards, being maximum in position P2.
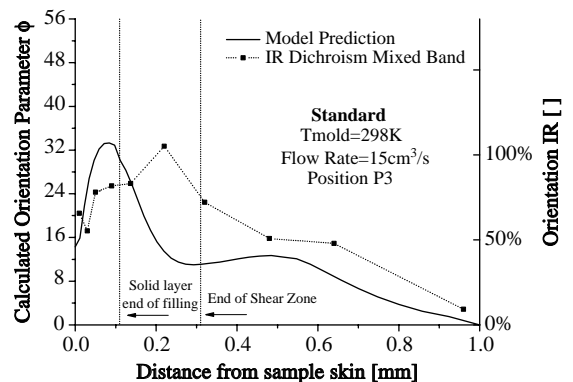

Fig. 27. Orientation distribution along thickness as determined by analysis of IR spectra for 'standard' sample in P3. Results of simulations are also shown as full lines (Section 5.3).
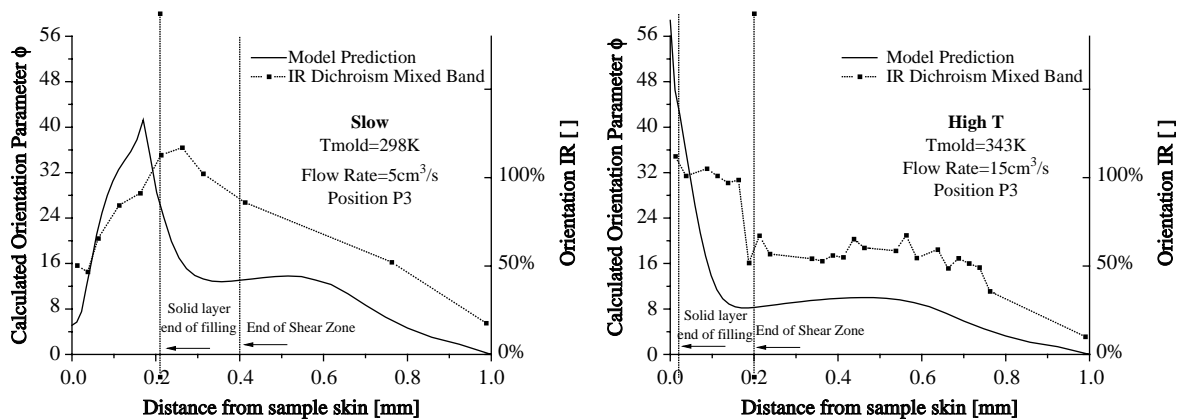
Fig. 28. Orientation distribution along thickness as determined by analysis of IR spectra for 'slow' and 'high T' samples in P3. Results of simulations are also shown as full lines (Section 5.3).

4.5.3. Direction of orientation

Distribution along thickness of the angle between direction of molecular orientation and flow direction in position P3 is reported in Fig. 30 for 'Standard' and in Fig. 31 for 'Slow' and 'High T' samples.

Figs. show that in layers close to the wall the orientation angle is smaller (smaller than 10°), namely the direction of orientation is nearly parallel to the main flow direction, this is consistent with a high level of orientation. In positions close to the sample midplane, where the orientation becomes smaller, the direction of orientation rotates increasing the angle with the main flow direction.

5. Simulation

Molding experiments were simulated in this work by means of a code developed at University of Salerno [15]. Being an 'open' code, this software easily allows
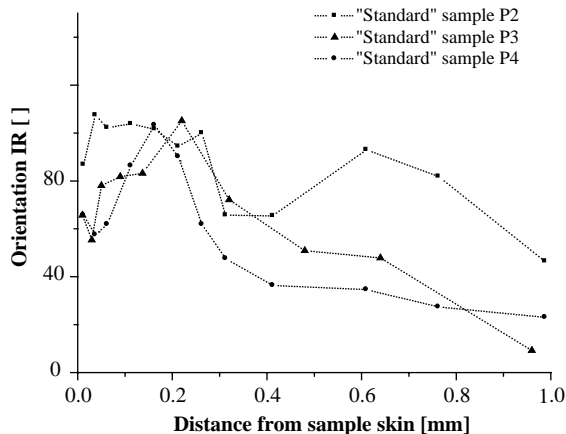
modifying fields and constitutive equations to account for aspects usually neglected by commercial codes. In fact the Kolmogoroff–Avrami–Nakamura kinetic model was introduced in this simulation code with the aim of describing crystallization kinetics and morphology evolution.

Pressure evolutions during the process final distributions of crystallinity, molecular orientation and spherulite diameters have been simulated using the software code developed at University of Salerno, and simulation results have been compared with the data illustrated in the previous section. The code is based on Lord and Williams model and its extensions [107]. Axial convection, transverse conduction and heat generation, both viscous and due to heat of crystallization, are kept into account in the energy balance, together with the accumulation term. Lubrication approximation is adopted for

Fig. 29. Molecular orientation distribution along thickness in P2, P3 and P4 for 'standard' sample.

Fig. 30. Experimental and simulated distribution along thickness of the angle of average molecular orientation with respect to flow direction in 'standard' samples (Section 5.3).
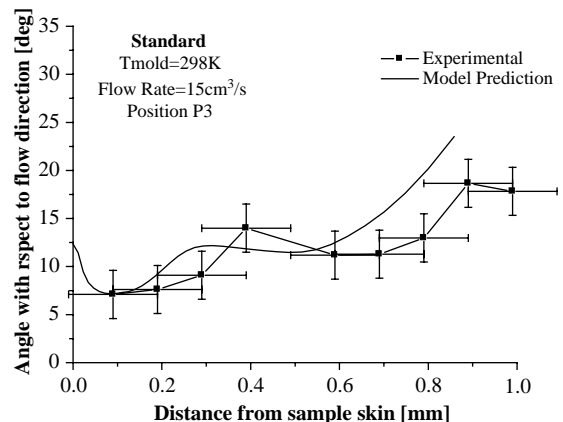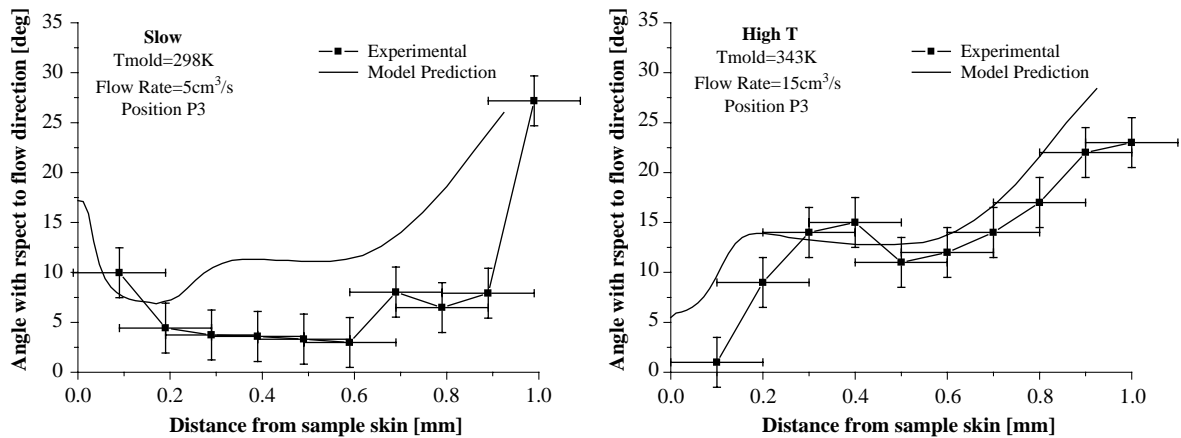
Fig. 31. Experimental and simulated distribution along thickness of the angle of average molecular orientation with respect to flow direction in the 'slow' and the 'high T' samples (Section 5.3).

the momentum balance. Complex geometries are obtained combining (in series or in parallel) simple cylindrical and rectangular elements. Knowledge of inlet injection temperature, zero heat flux at symmetry axis (and plane) and heat transfer coefficient at mold wall as a function of time are assumed as thermal boundary conditions. Density changes are neglected in the simulation of the filling step and in the post-filling steps are obtained as a combination of the densities of the different phases, each of them considered function of temperature and pressure. Mold deformation due to high cavity pressure is also kept into account. Further details about the model can be found elsewhere ([24]).

The quiescent crystallization kinetic and morphology evolution models described in Section 2 was implemented in the software. As mentioned above, this model describes morphology development in the whole cooling rate range of interest for injection molding, accounts also of the mesomorphic phase, but it neglects the effect of flow on crystallization kinetics.

As far as the description of molecular orientation is concerned, the non-linear dumbbell model proposed by Pantani et al. [20] and described in Section 1.1.5 has been adopted.

5.1. Pressure curves

Simulated and experimental pressure curves for all transducers are reported in Figs. 5 and 6. Results show that pressure evolutions were satisfactorily described at all transducer positions, at least for the 'standard' and 'High T' samples. The comparison regarding the 'Slow' sample deserves however some comments, since the pressure drop between positions P1 and P2

(namely across the gate) is underestimated during the packing step (i.e. after about 5 s). As mentioned in Section 4.2, the slow sample experiences the effect of flow on crystallization to a higher extent with respect to the other two conditions. This means that the polymer during the packing step could be more crystalline (and thus much more viscous) than model predictions, as the model adopted neglects the effect of flow on crystallization kinetics. Considering the quite good results obtained for the other two conditions, which can be taken as an evidence that the code well describes all relevant features of thermomechanical history experienced by the polymer during the molding tests, flow-induced crystallization can well be the cause of the underestimation of the pressure drop across the gate found for the 'slow' sample.

5.2. Morphology distribution

Experimental average spherulites diameter distribution along thickness in P3 is compared with model predictions in Figs. 15 and 16. Description of data is satisfactory in internal layers (closer to the midplane); of course the (quiescent) crystallization model predicts the presence of spherulites also in the shear zone (whose internal edge is marked by a vertical dotted line in figures) where SEM and AFM analysis revealed that spherulitic structures are replaced by fibers. In agreement with experimental observations, the biggest spherulites are in the core region and become smaller and smaller from the core region toward the skin. This can be associated with the evolution of temperature profile during the process: spherulites at the locations closer to the mold wall undergo higher cooling rates, spherulite growth has smaller time to proceed,

nucleation density becomes large and final spherulite dimensions remain small, because they are limited by impingement. At the locations near the centre, cooling rate is much smaller, spherulites have time to grow with low nucleation density and reach larger dimensions before impingement.

Also in positions P2 and P4 the description of data is satisfactory, obviously not close to sample skin where spherulitic structures are replaced by fibrils.

It can be noticed that simulation results systematically overestimate experimental data of spherulite diameters. Indeed this should be expected on the basis of a simple reasoning: the kinetic model adopted in the simulation disregards the effect of flow on crystallization, which causes an enhancement of nucleation and thus a reduction of final spherulite dimensions. Thus, the difference between simulations and data should increase on increasing the orientation level. As reported in Section 4.5, a certain degree of orientation is always present in molded samples, and this should obviously have an effect of final diameters. In order to stress this effect, in Fig. 32 the ratio between the spherulite diameters determined experimentally and that predicted by the simulation on the basis of the quiescent crystallization morphology evolution model, is reported for all positions along thickness and for all samples analyzed against the orientation degree as measured by IR. Despite of the large scattering, it is clear that the effect of orientation is toward a reduction of spherulite dimensions.

5.3. Molecular orientation

5.3.1. Molecular orientation distribution along thickness direction

The maximum eigenvalue of the deformation tensor $\underline{\underline{A}}$, denoted by ϕ in the present work, is a suitable index

of molecular orientation [20]. Comparison between experimental and predicted distribution of molecular orientation along thickness direction in position P3 is reported in Figs. 27 and 28. Results well predict a highly oriented zone in correspondence of the shear zone for all samples analyzed and a pronounced maximum close to the position of the layers which solidify last during filling. In the same figures a dotted vertical line indicates the position of the layer which solidifies last during the filling step, solidification condition being identified when overall crystallinity degree reaches 2%. It is worth noticing that the shear zone is thicker than the layers solidified during filling, and this holds true for all molding conditions and at all transducer positions. This is more clearly shown in Fig. 33, which also reveals a close relation between the thickness of the layer δ, skin and shear layers, and the thickness of the layer solidified during filling, as calculated by the simulation code.

5.3.2. Molecular orientation distribution along flow direction

Comparison between experimental and predicted distribution of molecular orientation along thickness direction in the other positions (P2 and P4) for the 'standard' sample is reported in Fig. 34. Results well predict that orientation parameter decreases on increasing the distance from the gate. On increasing distance from the gate, the time, the material undergoes filling flow becomes shorted and the packing flow rate reduces; both conditions contribute to keep molecular orientation low. The model well predicts the highly oriented zone in correspondence of the shear zone for all samples analyzed and is also able to describe the double maximum present in position P2 for all samples.
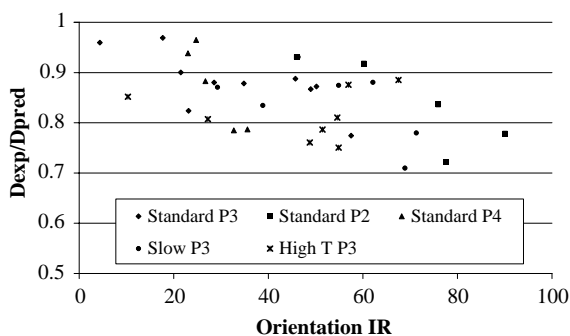
Fig. 32. Dependence of the ratio between experimental and predicted spherulite diameters versus the local orientation degree as measured by IR. Predictions are performed neglecting the effect of flow on crystallization kinetics.
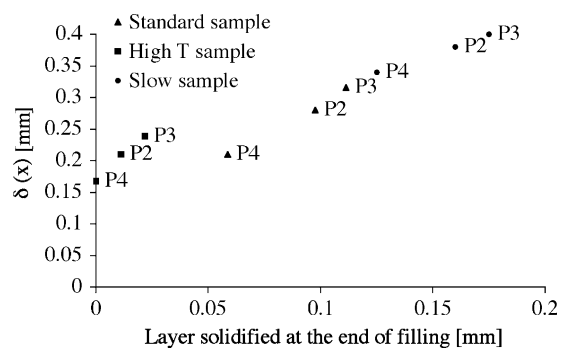
Fig. 33. Relationship between the oriented layer δ and the thickness of the layer solidified at the end of filling (as predicted by simulations).
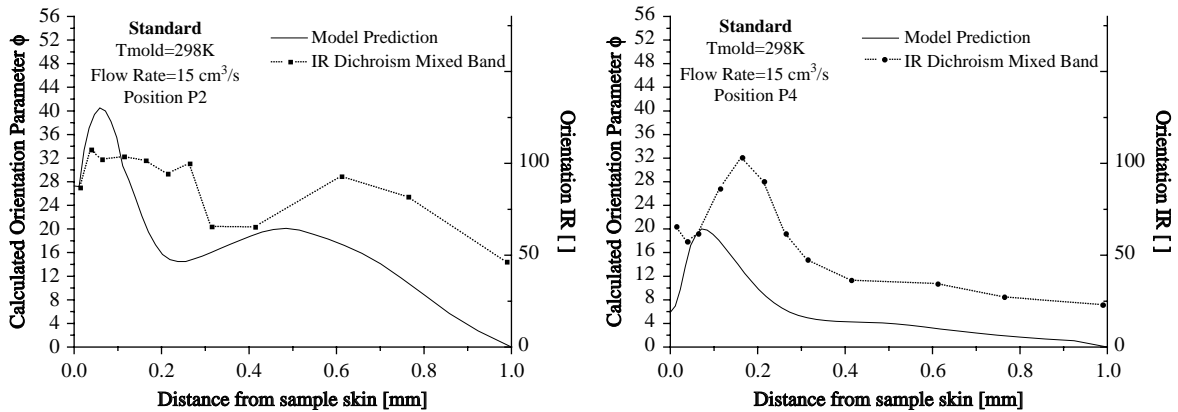
Fig. 34. Orientation distribution along thickness as determined by analysis of IR spectra for 'Standard' sample in P2 and P4. Results of simulations are also shown as full lines (Section 5.3).

5.3.3. Direction of orientation

Comparison between experimental and predicted distributions along thickness of the angle in position P3 between direction of molecular orientation and main flow direction is reported in Fig. 30 for 'Standard' samples and in Fig. 31 for 'Slow' and 'High T' samples. Model predictions are less sensitive to molding conditions with respect to experimental data. However, the main features of experimental results are captured for all conditions. Both experimental and simulation results indicate that the orientation direction is closer to the main flow direction on increasing levels of orientation.

5.4. Crystallinity distribution

A comparison between experimental data and model predictions of relative amount of the phases present is considered in Fig. 21 for 'standard' sample and in Fig. 22 for 'Slow' and 'High T' samples, respectively. As mentioned above even the high cooling rates at the sample skin do not have a quenching effect on the final polymer structure; this means that the crystallization kinetics on the overall (α plus mesomorphic) is such that the polymer crystallizes completely to an equilibrium state, either during the cooling or afterwards at the mold temperature. Predictions of overall (α plus mesomorphic phases) crystallinity degree discriminate between the two possibilities and show that crystallization takes place during cooling.

The final overall crystallinity distribution nicely compare with experimental results (Figs. 21 and 22 for position P2) as it is essentially constant along thickness. However, X-ray analysis reveal that final crystallinity is mostly in the α form, also close to sample skin, and crystallinity of the mesomorphic phase remains small

also at the sample skin. Vice versa, the quiescent crystallization model adopted in the simulation predicts a prevalence of the mesomorphic form at sample skin. Similar results were obtained by comparing experimental data of relative amount of the phases and model predictions in the other positions (P2 and P4), for all samples considered. A complete description of microstructure development during injection molding passes through a deeper understanding of the effect of flow on crystallization and morphology evolution; such a description certainly requires the modeling of main features of molecular dynamics and orientation development, which in this work was successfully carried out by a simple model.

Some discrepancy between simulation and experimental results at the sample skin was expected, since the effect of flow on crystallization kinetics (which at the sample skin reaches the maximum strength, both shear rates and orientation levels being maximum there) was not accounted for in the simulation. The discrepancies shown in Figs. 21 and 22 between fractions of α and mesomorphic phases at the sample skin can be overcome only by including an effect of flow on crystallization kinetics, which has to be more effective on the kinetics of the α phase than on the kinetics on the mesophase.

6. Conclusions

The description of morphology evolution in injection molding is a very complex task. The most relevant aspects have been italized and discussed in this paper with reference to the state of the art and focusing the attention on isotactic polypropylene. Main points are summarized below.

The description of morphology evolution has to keep into account nucleation and crystal growth and all crystalline phases (including mesophases) have to be considered as competing for the same molten polymer. In order to describe morphology evolution during injection molding, the polymer has to be characterized in the range of cooling rates and pressure characteristic of the processes, namely 1–1000 °C/s and several hundred bars.

Commercial iPP resins usually undergo heterogeneous nucleation, which is satisfactorily described by a nucleation density, which is a decreasing function of temperature. As either crystallization temperature decreases or cooling rate from the melt increases, nucleation density increases and thus final spherulite dimensions decreases.

Nucleation densities and growth rates of iPP (determined under isothermal conditions and low undercooling) is found to be consistent with density and morphology of samples crystallized under cooling rates as high as those encountered during processing operations (several hundreds of Kelvin degrees per second) only if the kinetics of mesomorphic phase is accounted for ([41]). Under quiescent conditions and cooling rates higher than about 50 K/s mesomorphic crystallization takes place at a faster rate than crystallization of the α phase toward spherulites; under higher cooling rates spherulites do not impinge against each other and under cooling rates of a few hundreds of K/s spherulites do not form at all, while only mesomorphic phase forms.

Kinetics and morphology of crystallization are drastically affected by the morphology determined in the melt by effect of flow (flow field and crystallization are thus coupled). The identification of a measure of melt structure, adequate to describe the effect of flow on the crystallization kinetics and morphology evolution during crystallization, is still under discussion. According to the literature, the parameters describing orientation (and stretch of the melt) and the recoverable strain can be representative of melt morphology; thus they can properly be adopted to describe the effect of flow and should be considered good candidates for describing the effect of flow on crystallization kinetics and morphology evolution.

Information in the literature indicate that, above a critical shear rate, crystallization kinetics increases and from a slightly oriented melt a much more oriented crystalline phase is often solidified. Above a higher critical shear rate value crystallization changes from spherulitic to fibrillar. Obviously, a comprehensive analysis would clarify that the critical values pertain to a melt structural variable rather than to the shear rate.

Growth rate seems to be affected by the flow [90], however to an extent smaller than nucleation.

The development of melt morphology by effect of flow is a phenomenon difficult to describe as rheological parameters are function of temperature and pressure and in their turn of melt morphology.

An ideal rheological model for the evolution of melt morphology should be simple, easily handled in a software, and it should have as output the evolution of parameters describing orientation and stain.

Rheological parameters are obviously function of crystallinity (second coupling mechanism between evolution of crystallinity and rheology); during crystallization some rheological parameters undergo a change of several orders of magnitude. The effect of crystallinity on viscosity is a very important subject in the analysis of polymer processing operations: a deeper investigation is required in that field, both from experimental and from modeling points of view. Currently an abrupt increase of viscosity is reported when crystallinity reaches a 'critical' value, literature information about the critical crystallinity values is controversial.

The effect of flow on crystallization kinetics has been object of several papers and also several models have been proposed, the comparison regards always sets of data which are satisfactorily described by any of the models but in the same time do not allow to discriminate between them.

An iPP resin already well characterized as far as rheological behavior and quiescent crystallization kinetics under a very wide range of cooling conditions (up to several hundred K/s) is considered in this work to show an example of morphology evolution during injection molding.

The resin was injected and morphology distribution in the moldings was carefully investigated as far as the thickness of the shear layer on the molding skin, spherulitic diameter and phase content (amorphous, α and mesomorphic) as function of the distance from the skin; also, orientation was measured as function of both distance from the skin and main flow direction.

The parameters for crystalline morphology evolution were determined accounting of both α and mesomorphic phases, but neglecting the effect of flow on crystallization kinetics; a simple non-linear dumbbell model was adopted to describe the morphology evolution of the melt. The comparison between the results of the morphology distribution analysis and simulation results shows that:

- beyond an oriented layer close to sample skin, main features of distributions of spherulites radii, crystallinity of α and mesomorphic phases are satisfactory predicted on the basis of nucleation density and growth rate of α spherulites and of kinetics of a competing mesomorphic phase, all calibrated on the basis of data obtained over a wide range of quiescent crystallization conditions;

- both experimental data and the simulation results show the existence of a high orientation layer close to the sample skin, and a decrease of orientation toward the central zone where a lower maximum may be determined by the packing flow, if it is sufficiently intense;

- the morphology is essentially fibrillar in the highly oriented layer (called shear layer) and spherulitic toward the sample midplane; results of the simulation show that a relevant part of this layer solidifies after mold filling;

- the thicknesses of both the shear layer and the layer solidified during mold filling increase as either flow rate or mold temperature decrease, and there is a correlation between the two;

- spherulite diameters increase from the shear layer toward the sample midplane; values predicted for final spherulite diameters are higher than experimental values, and the ratio increases on increasing the local orientation level, consistently with the hypothesis that, by effect of orientation, nucleation increases and thus spherulite dimensions decrease;

- total crystallinity (α+mesomorphic) was found constant over the whole sample thickness by both the sample characterization and the simulation results on the basis of the quiescent kinetic crystallization;

- results of simulation predict also a sharp decrease of the fraction of the α phase on the sample skin, whereas experimentally the α phase is found essentially constant over the whole sample cross-section, including the layers very close to the skin, which present a high level of orientation. This suggests that the effect of orientation should be toward an enhancement above all of the kinetics toward the α phase;

- an enhancement of crystallization by effect of flow would also give rise to an increase of prediction for pressure drop through the gate, consistently with experimental curves of Figs. 5 and 6.

Eventually, it should be considered that the next step to make is to introduce the effect of flow on crystallization kinetics.

References

[1] Cakmak M, Hsiung CM, Wang YD. Structure development in injection molding of semicrystalline polymers. Japan: Shiguma Syuppan Publisher; 1997.

[2] Kantz MR, Newman JR, Stigale FH. The skin-core morphology and structure–property relationships in injection-moulded polypropylene. J Appl Polym Sci 1972;16: 1249–60.

[3] Menges G, Wubken G, Horn B. Effect of the processing conditions on the crystallinity and morphological structure of partially crystalline injection moldings. Colloid Polym Sci. 1976;254(3):267–78.

[4] Fujiyama M, Wakino T, Kavasaki Y. Structure of skin layer in injection-molded polypropylene. J Appl Polym Sci 1988;35(1): 29–49.

[5] Wenig W, Herzog F. Injection molding of polypropylene: X-ray investigation of the skin-core morphology. J Appl Polym Sci 1993;50:2163–71.

[6] Saiu M, Brucato V, Piccarolo S, Titomanlio G. Injection molding of isotactic polypropylene (iPP). An integrated experimental investigation. Int Polym Process 1992;7(3): 267–73.

[7] Kalay G, Bevis MJ. Processing and physical property relationships in injection-molded isotactic polypropylene, 2. Morphology and crystallinity. J Polym Sci Part B: Polym Phys 1997;35:265–91.

[8] Liu G, Edward G. Correlation between morphology distribution of injection molded polypropylene and processing history identified by numerical simulation. J Injection Molding Technol 2001;5(3):133–40.

[9] Viana JC, Cunha AM, Billon N. The thermomechanical environment and the microstructure of an injection moulded polypropylene copolymer. Polymer 2002;43(15):4185–96.

[10] Mendoza R, Regnier G, Seiler W, Lebrun JL. Spatial distribution of molecular orientation in injection molded iPP: influence of processing conditions. Polymer 2003;44(11): 3363–73.

[11] Kamal MR, Kenig S. The injection moulding of thermoplastic. Part I: Theoretical model. Polym Eng Sci 1972;12:294–301.

[12] Hieber CA, Shen SF. A finite element-/finite difference-simulation of the injection moulding filling process. J Non-Newton Fluid Mech 1980;7:1–32.

[13] Chiang HH, Hieber CA, Wang KK. A unified simulation of the filling and post filling stages in injection moulding. Part I: formulation. Polym Eng Sci 1991;31:116–24.

[14] Kennedy P. Flow analysis of injection moulding. Munich: Hanser; 1995.

[15] Titomanlio G, Speranza V, Brucato V. On the simulation of thermoplastic injection molding process. Part 2. Relevance of interaction between flow and crystallisation. Int Polym Proc 1997;12(1):45–53.

[16] Pichelin E, Coupez T. Finite element solution of the 3D mold filling problem for viscous incompressible fluid. Comput Methods Appl Mech Eng 1998;163:359–71.

[17] Zheng R, Kennedy P, Phan-Thien N, Fan X-J. Thermoviscoelastic simulation of thermally and pressure-induced stresses in injection moulding for the prediction of shrinkage and warpage for fiber-reinforced thermoplastics. J Non-Newton Fluid Mech 1999;84(2–3):159–90.

[18] Ilinca F, Hetu JF. Three-dimensional filling and post-filling simulation of polymer injection molding. Int Polym Process 2001;16(3):291–301.

[19] Barriere T, Gelin JC, Liu B. Improving mould design and injection parameters in metal injection moulding by accurate 3D finite element simulation. J Mater Process Technol 2002; 125-126:518–24.

[20] Pantani R, Sorrentino A, Speranza V, Titomanlio G. Molecular orientation in injection molding: experiments and analysis. Rheol Acta 2004;43:109–18.

[21] Douven LFA, Baaijens FTP, Meijer HEH. The computation of properties of injection-moulded products. Prog Polym Sci 1995;20:403–57.

[22] Zuidema H, Peter WMP, Meijer HEH. Development and validation of a recoverable strain-based model for flow-induced crystallization of polymers. Macromol Theory Simul 2001;10(5):447–60.

[23] Kim IH, Park SJ, Chung ST, Kwon TH. Numerical modelling of injection compression moulding for center gated disk. Part I. Injection moulding with viscoelastic compressible fluid. Polym Eng Sci 1999;39:1930–42.

[24] Pantani R, Speranza V, Titomanlio G. Relevance of mold-induced thermal boundary conditions and cavity deformation in the simulation of injection molding. Polym Eng Sci 2001; 41(11):2022–35.

[25] Hieber CA. Modeling/simulating the injection molding of isotactic polypropylene. Polym Eng Sci 2002;42(7):1387–409.

[26] Isayev AI, Guo X, Guo L, Demiray M. Microstructure of injection moldings of isotactic polypropylenes with various molecular weights: simulation and experiment. Annu Tech Conf- Soc Plast Eng 1997;2(55):1517–21.

[27] Delaunay D, Le Bot P, Fulchiron R, Luye JF, Regnier G. Nature of contact between polymer and mold in injection moulding. Part II: Influence of mold deflection on pressure history and shrinkage. Polym Eng Sci 2000;40:1692–700.

[28] Flaman AAM. Build-up and relaxation of molecular orientation in injection molding. PhD thesis. THEindhoven (NL); 1990.

[29] Kamal MR, Goyal SK, Chu E. Simulation of injection mold filling of viscoelastic polymer with fountain flow. AIChE J 1988;34(1):94–106.

[30] Mavridis H, Hrymak AN, Vlachopoulos J. The effect of fountain flow on molecular orientation in injection molding. J Rheol 1988;32(6):639–63.

[31] Fauchon D, Dannelongue HH, Tanguy PA. Numerical simulation of the advancing front in injection molding. Int Polym Process 1991;6(1):13–18.

[32] Coyle DJ, Blake JW, Macosko CW. The kinematics of fountain flow in mould filling. AIChE J 1987;33:1168–77.

[33] Schultz JM. Roles of 'solute' and heat flow in the development of polymer microstructure. Polymer 1991;32(18):3268–83.

[34] Lafleur PG, Kamal MR. A structure-oriented computer simulation of the injection molding of viscoelastic crystalline polymers. Part I: Model with fountain flow, packing, solidification. Polym Eng Sci 1986;26(1):92–101.

[35] Papathanasiou TD. Modelling of injection mould filling: effect of undercooling on polymer crystallization. Chem Eng Sci 1995;50(21):3433–42.

[36] Han S, Wang KK. Shrinkage prediction for slowly crystallizing thermoplastic polymers in injection molding. Int Polym Process 1997;12(3):228–37.

[37] Ito H, Minagawa K, Takimoto J, Tada K, Koyama K. Effect of pressure and shear stress on crystallization behaviors in injection molding. Int Polym Process 1996;11(4):363–8.

[38] Manzione LT. Crystallization in injection moulding. ANTEC 1987;285–8.

[39] Brucato V, Piccarolo S, Titomanlio G. Crystallization kinetics in relation to polymer processing. Makromol Chem, Macromol Symp 1993;68:245–55.

[40] Coccorullo I, Pantani R, Titomanlio G. Crystallization kinetics and solidified structure in iPP under high cooling rates. Polymer 2003;44(1):307–18.

[41] Mezghani K, Phillips PJ. The γ-phase of high molecular weight isotactic polypropylene: III. The equilibrium melting point and the phase diagram. Polymer 1998;39(16):3735–44.

[42] Hoffman JD, Lauritzen JI. Crystallization of bulk polymers with chain folding: theory of growth of lamellar spherulites. J Res Natl Bur Stand 1961;65A:297–336.

[43] Guo X, Isayev AI, Guo L. Crystallinity and microstructure in injection moldings of isotactic polypropylenes. Part 1: a new approach to modeling and model parameters. Polym Eng Sci 1999;39(10):2096–114.

[44] Sudduth RD, Yarala PK, Sheng Qin. A comparison of induction time and crystallization rate for syndiotactic polystyrene. Polym Eng Sci 2002;42(4):694–706.

[45] Sifleet WL, Dinos N, Collier JR. Unsteady-state heat transfer in a crystallizing polymer. Polym Eng Sci 1973;13(1):10–16.

[46] Hieber CA. Correlation for the quiescent crystallization kinetics of isotactic polypropylene and polyethyleneterephthalate. Polymer 1995;36(7):1455–67.

[47] Bourrigaud S, Marin G, Poitou A. Shear modification of long-chain branched polymers: a theoretical approach using the pom-pom model. Macromolecules 2003;36(4):1388–94.

[48] Eder G, Janeschitz-Kriegl H. Crystallization. In: Meijer HEM, editor. Materials science and technology, vol. 18. New York: Wiley; 1997.

[49] Kolmogoroff AN. On the statistic of crystallization development in metals. Isvest Akad Nauk SSSR Ser Math 1937;1:335.

[50] Angello C, Fulchiron R, Douilard A, Chabert B, Fillit R, Vautrin A, et al. Crystallization of isotactic polypropylene under high pressure (gamma Phase). Macromolecules 2000;33: 4138–45.

[51] Pantani R, Speranza V, Coccorullo I, Titomanlio G. Morphology of injection moulded iPP samples. Macromol Symp 2002;185:309–26 [Flow-induced crystallization of polymers].

[52] Watanabe K, Suzuki T, Masubuchi Y, Taniguchi T, Takimoto J, Koyama K. Crystallization kinetics of polypropylene under high pressure and steady shear flow. Polymer 2003; 44(19):5843–9.

[53] Zuidema H, Peters GWM, Meijer HEH. Influence of cooling rate on pVT-data of semicrystalline polymers. J Appl Polym Sci 2001;82(5):1170–86.

[54] Pogodina NV, Winter HH. Polypropylene crystallization as a physical gelation process. Macromolecules 1998;31(23): 8164–72.

[55] Vleeshouwers S, Meijer HEH. A rheological study of shear induced crystallization. Rheologica Acta 1996;35(5):391–9.

[56] Swarties FHM. Stress induced crystallization in elongational flow. PhD thesis. THEindhoven (NL), 2001.

[57] Boutahar K, Carrot C, Guillet J. Polypropylene during crystallization from the melt as a model for the rheology of molten-filled polymers. J Appl Polym Sci 1996;60(1):103–14.

[58] Floudas G, Hilliou L, Lellinger D, Alig I. Shear-induced crystallization of poly(e-caprolactone). 2. Evolution of birefringence and dichroism. Macromolecules 2000;33(17): 6466–72.

[59] Wassner E, Maier RD. Shear-induced crystallization of polypropylene melts. Proceedings of the international congress on rheology, 13th, Cambridge, UK; 2000.

[60] Pantani R, Speranza V, Titomanlio G. Relevance of crystallisation kinetics in the simulation of the injection molding process. Int Polym Process 2001;16(1):61–71.

[61] Pogodina NV, Lavrenko VP, Srinivas S, Winter HH. Rheology and structure of isotactic polypropylene near the gel point: quiescent and shear-induced crystallization. Polymer 2001; 42(21):9031–43.

[62] Acierno S, Grizzuti N. Measurements of the rheological behavior of a crystallizing polymer by an 'inverse quenching' technique. J Rheol 2003;47(2):563–76.

[63] Lin YG, Mallin DT, Chien JCW, Winter HH. Dynamic mechanical measurement of crystallization-induced gelation in thermoplastic elastomeric poly(propylene). Macromolecules 1991;24(4):850–4.

[64] Gupta RK. Particulate suspensions. In: Flow and rheology in polymer composites manufacturing. Amsterdam: Elsevier; 1994.

[65] Metzner AB. Rheology of suspensions in polymeric liquids. J Rheol 1985;29(6):739–75.

[66] Katayama K, Yoon MG. Polymer crystallization in melt spinning: mathematical simulation. High-speed fiber spinning 1985 p. 207–223.

[67] Ziabicki A. The mechanisms of 'neck-like' deformation in high-speed melt spinning. 2. Effects of polymer crystallization. J Non-Newton Fluid Mech 1988;30(2–3):157–68.

[68] Guo J, Narh KA. Computer simulation of stress-induced crystallization in injection molded thermoplastics. Polym Eng Sci 2001;41(11):1996–2012.

[69] Shimizu J, Okui N, Kikutani T, et al. Simulation of dynamics and structure formation in high-speed melt spinning. In: Ziabicki A, Kawai H, editors. High-speed fiber spinning. New York: Wiley; 1985. p. 173.

[70] Tanner R. A suspension model for low shear rate polymer solidification. J Non-Newton Fluid Mech 2002;102(2): 397–408.

[71] Tanner R. On the flow of crystallizing polymers. I. Linear regime. J Non-Newton Fluid Mech 2003;112(2-3): 251–68.

[72] Poitou A, Ammar A, Marco Y, Chevalier L, Chaouche M. Crystallization of polymers under strain: from molecular properties to macroscopic models. Comput Methods Appl Mech Eng 2003;192:3245–64.

[73] Verbeeten WMH, Peters GWM, Baaijens FPT. Differential constitutive equations for polymer melts: the extended pompom model. J Rheol 2001;45(4):823–43.

[74] Isayev AI, Hieber CA. Toward a viscoelastic modeling of the injection molding of polymers. Rheologica Acta 1980;19(2): 168–82.

[75] Baaijens FPT, Douven LFA. In: Dijksman JF, Nieuwstadt FTM, editors. Integration of theory and applications in applied mechanics. Doerdrecht: Kluwer; 1990. p. 73–90.

[76] Pantani R, Speranza V, Sorrentino A, Titomanlio G. Molecular orientation and strain in injection moulding of thermoplastics. Macromol Symp 2002;185:293–307 [Flow-induced crystallization of polymers].

[77] Barnes HA, Roberts GP. A simple empirical model describing the steady-state shear and extensional viscosities of polymer melts. J Non-Newton Fluid Mech 1992;44:113–26.

[78] Keller A, Kolnaar HWH. Flow induced orientation and structure formation. In: Meijer HEH, editor. Processing of polymers, vol. 18. Weinheim, Germany: VCH; 1997.

[79] Lamberti G, Titomanlio G. Evidences of flow induced crystallization during characterized film casting experiments. Macromol Symp 2002;185:167–80 [Flow-induced crystallization of polymers].

[80] Ziabicki A, Kawai H. High speed fiber spinning. New York: Wiley; 1985.

[81] Doufas AK, McHugh AJ, Miller C, Immaneni A. Simulation of melt spinning including flow-induced crystallization Part II. Quantitative comparisons with industrial spinline data. J Non-Newton Fluid Mech 2000;92:81–103.

[82] Kulkarni JA, Beris AN. Lattice-based simulations of chain conformations in semi-crystalline polymers with application to flow-induced crystallization. J Non-Newton Fluid Mech 1999; 82:331–66.

[83] Ziabicki A. Crystallization of polymers in variable external conditions. Part 4. Isothermal crystallization in the presence of variable tensile stress or hydrostatic pressure. Colloid Polym Sci 1999;277(8):752–61.

[84] Flory PJ. Thermodynamics of crystallization in high polymers. I. Crystallization induced by stretching. J Chem Phys 1947;15: 397–408.

[85] Haas TW, Maxwell B. Effects of shear stress on the crystallization of linear polyethylene and poly-1-butene. Polym Eng Sci 1969;9(4):225–41.

[86] Guo J, Narh KA. Simplified model of stress-induced crystallization kinetics of polymers. Adv Polym Technol 2002;21(3): 214–22.

[87] Titomanlio G, Lamberti G. Modeling flow induced crystallization in film casting of polypropylene. Rheologica Acta 2004;43(2):146–58.

[88] Kim KH, Isayev AI, Keehae Kwon. Flow-induced crystallization in the injection molding of polymers: a thermodynamic approach. J Appl Polym Sci 2005;95(3):502–23.

[89] Peters GWM, Zuidema Hans, Meijer HEH. A viscoelastic based model for flow induced crystallisation. Proceedings of the international congress on Rheology, vol. 1, 13th, Cambridge, UK; 2000, p. 304–306.

[90] Duplay C, Monasse B, Haudin JM, Costa JL. Shear-induced crystallization of polypropylene: influence of molecular weight. J Mater Sci 2000;35:6093–103.

[91] Lee O, Kamal MR. Experimental study of post-shear crystallization of polypropylene melts. Polym Eng Sci 1999;39(2): 236–48.

[92] Tribout C, Monasse B, Hausin JM. Experimental study of shear-induced crystallization of an impact polypropylene copolymer. Colloid Polym Sci 1996;274(3):197–208.

[93] Koscher E, Fulchiron R. Influence of shear on polypropylene crystallization: morphology development and kinetics. Polymer 2002;43(25):6931–42.

[94] Acierno S, Coppola S, Grizzuti N, Maffettone PL. Coupling between kinetics and rheological parameters in the flow-induced crystallization of thermoplastic polymers. Macromol Symp 2002;185:233–41.

[95] Zheng R, Kennedy PK. A model for post-flow induced crystallization: general equations and predictions. J Rheol 2004;48(4):823–42.

[96] Progelhof CR. Polymer Engineering Principles. Munich: Hanser; 1993.

[97] La Carrubba V, Brucato V, Piccarolo S. Isotactic polypropylene solidification under pressure and high cooling rates. A master curve approach. Polym Eng Sci 2000;40(11):2430–41.

[98] Couch MA, Binding DM. High pressure capillary rheometry of polymeric fluids. Polymer 2000;41(16):6323–34.

[99] Laun HM. Prediction of elastic strains of polymer melts in shear and elongation. J Rheol 1986;30(3):459–501.

[100] Grizzuti N. Personal Communication; 2005.

[101] White HM, Basset DC. On row structures, secondary nucleation and continuity in polypropylene. Polymer 1998; 39:3211–8.

[102] Hobbs JK, Winkel AK, McMaster TJ, Humphris ADL, Baker AA, Blakely S, et al. Some recent developments in SPM of crystalline polymers. Macromol Symp 2001;167:1–14 [Recent advances in scanning probe microscopy of polymers].

[103] Samuels RJ. Structured polymer properties. New York: Wiley; 1974.

[104] Murthy NS, Minor H. General procedure for evaluating amorphous scattering and crystallinity from X-ray diffraction scans of semicrystalline polymers. Polymer 1990;31(6): 996–1002.

[105] Coccorullo I. Morphology distribution in injection moulded Ipp samples. Phd thesis Salerno, 2002.

[106] Kumaraswamy G, Verma RK, Issaian AM, Wang P, Kornfield JA, Yeh F, et al. Shear-enhanced crystallization in isotactic polypropylene part 2. Analysis of the formation of the oriented 'skin'. Polymer 2000;41(25): 8931–40.

[107] Lord HA, Williams G. Mold-filling studies for the injection molding of thermoplastic materials. II. Transient flow of plastic materials in the cavities of injection-molding dies. Polym Eng Sci 1975;15(8):569–82.